TASHKENT STATE TECHNICAL UNIVERSITY AFTER ISLAM KARIMOV
NEW UZBEKISTAN UNIVERSITY

On the right of the manuscript

UDC: 530.12:531.51

01.03.01 - Astronomy

01.04.02 - Theoretical Physics

ALIMOVA ASALKHON

OPTICAL PROPERTIES AND DYNAMICS OF PARTICLES AROUND BLACK HOLES IN MODIFIED GRAVITIES

DISSERTATION OF THE DOCTOR OF PHILOSOPHY (PhD) IN PHYSICS AND MATHEMATICS

Supervisors:

Prof. Atamurotov Farruh Shukhratovich

Ahmedov Bahodir Babomurotovich

Tashkent-2025

List of Abbreviations

BH	Black Hole
GR	General Relativity
LIGO	Laser Interferometer Gravitational-Wave Observatory
LISA	Laser Interferometer Space Antenna
VEV	Vacuum Expectation Value
RN	Reissner–Nordström
ASG	Asymptotically Safe Gravity
KR	Kalb–Ramond
EHT	Event Horizon Telescope
ISCO	Innermost Stable Circular Orbit
MPD	Mathisson–Papapetrou–Dixon equations
SSC	Spin Supplementary Condition
TD	Tulczyjew–Dixon
RPM	Relativistic Precession Model
QPO	Quasi–Periodic Oscillation
PS	Photon Sphere
MCMC	Markov Chain Monte Carlo
OF	Orbital Frequency
REF	Radial Epicyclic Frequency
VEF	Vertical Epicyclic Frequency

Contents

INTRODUCTION

Topicality and demand of the theme of the dissertation.

The study of black holes and modified gravity theories is at the forefront of modern theoretical and observational astrophysics. With groundbreaking discoveries such as the first images of black hole shadows by the Event Horizon Telescope (EHT) and the detection of gravitational waves by LIGO-Virgo, there is a growing need to explore alternative theories of gravity that extend or modify General Relativity (GR). These theories aim to address unresolved issues in GR, such as singularities, dark matter, and dark energy, while providing testable predictions for future observations.

This dissertation systematically investigates the dynamics of particles and light in the vicinity of black holes within several modified gravity frameworks, including quantum-corrected black holes, Reissner–Nordström-like black holes in Kalb–Ramond gravity, and regular black holes arising from asymptotically safe gravity. Such research is highly relevant as it bridges theoretical predictions with observational data, offering insights into the nature of compact objects and their environments. The analysis of spinning particles, gravitational lensing in plasma and has direct implications for interpreting astrophysical phenomena, such as accretion disk dynamics, quasi-periodic oscillations (QPOs), and black hole shadows.

Furthermore, the demand for this work is underscored by ongoing and future observational missions, such as next-generation EHT upgrades, LISA, and X-ray

telescopes, which will probe strong-field gravity with unprecedented precision. By constraining parameters of modified gravity models through black hole observations, this research contributes to the broader effort to uncover deviations from GR and explore new physics. Thus, the dissertation aligns with cutting-edge astrophysical inquiries and supports the advancement of fundamental gravitational physics.

Moreover, the dissertation aligns with the strategic scientific priorities in Uzbekistan and the broader international community. This dissertation work corresponds to the tasks of the following state regulatory documents: Decree of the President of the Republic of Uzbekistan No. UP-4947 "On the Strategy of Actions for the Further Development of the Republic of Uzbekistan" dated February 07, 2017, Decree of the President of the Republic of Uzbekistan No. PP-2789 "On Measures for Further Improvement of Academy of Sciences, Organization, Management, and Financing of Research Activities from 18.02.2017.

Relevance of the research to the priority areas of science and technology development of the Republic of Uzbekistan. Dissertation research has been carried out in accordance with the priority areas of science and technology in the Republic of Uzbekistan: II. “Power, energy and resource-saving”.

Degree of study of the problem

The study of black holes and modified gravity theories has been a central focus in theoretical and observational astrophysics for decades. Classical black hole solutions in General Relativity (GR), such as the Schwarzschild and Kerr metrics, have been extensively analyzed in terms of particle dynamics and gravitational lensing (Atamurotov, Ahmedov, Toshmatov, Bambi). However, the limitations of GR—such as singularities, the lack of a quantum description, and discrepancies in cosmological observations—have motivated the exploration of alternative gravity

models. Modified theories, including quantum-corrected gravity, asymptotically safe gravity, and metric-Palatini extensions, have been proposed to address these issues, with varying degrees of investigation. While some aspects of these theories, such as their basic black hole solutions and stability conditions, have been studied (Atamurotov, Rayimbaev), the detailed behavior of particles and light in these spacetimes remains an active area of research.

The motion of spinning particles around black holes, governed by the Mathisson-Papapetrou-Dixon equations, has been examined in GR and some modified gravity scenarios (Mustafa, Rayimbaev, Herdeiro, Sotiriou). However, the effects of quantum corrections and additional fields (e.g., Proca fields or Kalb-Ramond backgrounds) on spinning particle dynamics are less explored. Similarly, gravitational lensing in plasma environments has been studied in standard GR (Bambi, Stuchlík, Tsupko, Bisnovatyi-Kogan, Mustafa, Rayimbaev), but its implications in modified gravity, particularly in the presence of Lorentz-violating terms or non-minimal couplings, require further investigation.

Despite significant progress, many aspects of these modified gravity theories remain underdeveloped. Observational constraints from black hole shadows, gravitational waves, and X-ray spectroscopy (Bambi, Frolov, Konoplya, Radu, Benavides-Gallego) provide new opportunities to test these models, but systematic studies linking theoretical predictions to measurable phenomena are still needed. This dissertation contributes to filling these gaps by analyzing particle dynamics and optical properties in specific modified gravity frameworks, thereby advancing our understanding of black holes beyond classical GR.

Connection of the topic of the dissertation with the scientific research of the higher educational research institutions, where the dissertation was carried out. The dissertation was done in the framework of

the scientific projects funded by the Ministry of Innovative Development: F-FA-2021-510 "Investigations of nuclear matter of neutron stars in modified gravity" (2021-2026).

The aim of the research is to probe modified gravity using analysis of black hole astrophysics via particles orbits and black hole shadows.

The tasks of the research:

- to analyze the dynamics of spinning particles using the Mathisson-Papapetrou-Dixon (MPD) equations;
- to determine the innermost stable circular orbit (ISCO), effective potential, and effective force, and study their dependence on the black hole's quantum-corrected parameter and the particle's spin;
- to examine the superluminal bound condition for spinning particles;
- to investigate weak gravitational lensing and shadow formation in Kalb-Ramond (KR) gravity;
- to analyze the effects of uniform and inhomogeneous plasma on photon trajectories and black hole shadows;
- to compare theoretical predictions with observational data from the Event Horizon Telescope (EHT) for Sgr A*;
- to examine the motion of neutral test particles around regular black holes;
- to derive expressions for energy, angular momentum, and stability of circular orbits;
- to investigate epicyclic oscillations, quasi-periodic oscillations (QPOs, and periastron precession;

- to analyze particle collisions and compute center-of-mass energy near the black hole;

- to compare black hole shadows with EHT data for M87* and Sgr A* to constrain model parameters;

The objects of the research are the physical phenomena and theoretical models describing the motion and optical behavior and astrophysical properties of particles and fields in the vicinity of black holes within various modified gravity frameworks.

The subjects of the research are the mathematical models, analytical methods, and computational techniques used to study spinning particle dynamics, black hole shadows, gravitational lensing in plasma environments and observational constraints on black hole properties in the context of modified gravity theories.

The methods of the research are analytical and numerical methods grounded in general relativity and modified gravity theories, including the Mathisson–Papapetrou–Dixon equations for spinning particle dynamics and geodesic analysis for photon trajectories for black hole systems. The study integrates effective potential analysis, stability criteria for circular orbits, and superluminal bound conditions, along with optical geometry techniques for shadow radius estimation and gravitational lensing in plasma media. Numerical simulations and graphical analysis are used to explore parameter dependencies and compare theoretical predictions with observational data from sources such as the Event Horizon Telescope.

The scientific novelty of the research is the following:

- A comprehensive analysis of spinning particle motion around quantum-corrected black holes was conducted, revealing the influence of quantum gravity param-

eters on effective potential, ISCO characteristics, and superluminal bounds.

- New results were obtained on the optical properties of Reissner–Nordström-like black holes in Kalb–Ramond gravity, including shadow radius and gravitational lensing effects in both homogeneous and inhomogeneous plasma environments.

Practical results are as follows:

- Developed theoretical models and computational tools for predicting observable signatures of modified gravity effects in black hole environments, applicable to interpreting Event Horizon Telescope data.
- Established parameter constraints for quantum-corrected and Lorentz-violating black holes based on black hole shadow observations, enabling their use as astrophysical tests of gravity theories.
- Provided a methodological framework for analyzing particle dynamics and lensing in modified gravities, which can be adapted for further astrophysical modeling and educational purposes.

Reliability of the research results are provided by the use of well-established theoretical frameworks, including general relativity, modified gravity theories, and the Mathisson–Papapetrou–Dixon formalism for spinning particle dynamics. The mathematical models and analytical derivations are based on rigorous physical principles, while numerical simulations were carried out using verified computational methods. The obtained results are consistent with known limiting cases, such as Schwarzschild and Kerr solutions, and have been cross-checked against observational constraints from the Event Horizon Telescope and other astrophysical data, confirming their physical plausibility and applicability.

The scientific and practical significance of the research results are the following

- Expands the theoretical understanding of particle dynamics and optical properties of black holes in modified gravity frameworks, contributing to the development of alternative gravitational models.

- Provides analytical and numerical tools for predicting observational signatures—such as black hole shadows, gravitational lensing patterns, and orbital dynamics—that can be directly compared with current and future astronomical data.

- Offers parameter constraints for quantum-corrected, Lorentz-violating, and vector-field–modified black holes, enabling their use as practical tests of gravity theories in astrophysical observations.

- Establishes a methodological basis applicable in further astrophysical research and higher education for modeling extreme gravitational environments, thereby supporting both scientific investigations and training of specialists in relativistic astrophysics.

Application of the research results.

The results of the study of the dynamics of particles around black holes in modified gravity theories have been applied as follows:

the theoretical research results and methods, published in the scientific paper "A. Alimova, Z. Turakhonov, F. Atamurotov, A. Abdujabbarov, Shadow and weak gravitational lensing of RN-like BH in plasma, Physics of the Dark Universe, Vol. 47, 101749 (2025), https://doi.org/10.1016/j.dark.2024.101749" and presented in the Doctorate (PhD) thesis of Ms. Asalkhon Alimova have been used in the

framework of the programs supported by Fudan University (Letter from Prof. Cosimo Bambi)

Approbation of the research results

The dissertation results have been discussed in 3 national conferences.

Publication of the research results

The principal results of the dissertation have been published in scientific journals and conference proceedings. A total of 11 scientific publications related to the dissertation topic have been produced, of which 6 articles appeared in international peer-reviewed journals recognized by the Supreme Attestation Commission of the Republic of Uzbekistan as appropriate outlets for the publication of PhD research results.

Volume and structure of the dissertation

Consists of an introduction, three chapters, a conclusion, and a list of references, all in 103 pages.

List of published papers

1. Mushtaq F., Tiecheng X., Ditta A., Atamurotov F., Abduvokhidov A., Alimova A., Weak gravitational lensing and fundamental frequencies of Einstein-Euler-Heisenberg black hole // New Astronomy 2024, Volume 108, article id. 102185 (№1 Web of Science, IF: 2.0).

2. Alimova A., Turakhonov Z., Atamurotov F., Abdujabbarov A., Shadow and weak gravitational lensing of RN-like BH in plasma // Physics of the Dark Universe 2025, Volume 47, article id. 101749 (№1 Web of Science, IF: 6.5).

3. Alimova A., Atamurotov F., Abdujabbarov A., Mustafa G., Channuie P. Impact of quantum-corrected parameter on spinning particle motion around a black hole // The European Physical Journal C 2025, Volume. 85, article number.646 (№1 Web of Science, IF: 4.8)

4. Mustafa G., Alimova A., Atamurotov F., Ibraheem A.A., Channuie P., Bahaddinova G., Testing regular black holes in the framework of asymptotically safe gravity using particle dynamics, QPOs, and shadow constraints // The European Physical Journal C 2025, Volume 85, article number. 741 (№1 Web of Science, IF: 4.8)

5. Alimova A., Ghorani E., Puliçe B., Atamuratov F, Abdujabbarov A., Thermodynamics of Einstein-Geometric Proca AdS Compact Objects// The European Physical Journal C, 2025, Volume.85, article number 962. (№1 Web of Science, IF: 4.8)

6. Ditta A.,Ashraf A.,Maurya. K.,Ali A.,Alimova A., Atamurotov F. Oscillatory motion and QPO signatures around rotating short-hairy black holes:

Bridging theory and observation//Physics of the Dark Universe 2025,Volume 50, article i.102071 (№1 Web of Science, IF: 6.5).

7. Davlataliyev A., Alimova A., Khamidov V., Gravitational lensing in Starobinsky-Bel-Robinson gravity in non-uniform plasma// O'zbekiston Milliy Universiteti xabarlari, 2024 [3/1/1], 471-473 betlar.

8. Alimova A., Abduqayumova G., Juraeva N., Spinning particles motion around the Reissner-Nordström-like black hole// O'zbekiston Milliy Universiteti xabarlari, 2025 [3/1/1], 403-406 betlar.

9. Ortiqboev D., Alimova A., Umaraliyev M., Photon motion in the Kalb-Ramond gravity // "Fizika fanining rivojida iste'dodli yoshlarning o'rni" Respublika ilmiy-amaliy konferensiya (RIAK-XVII-2024) materiallari to'plami: O'zMU,5-6-aprel,2024-yil. Toshkent.80-82 betlar.

10. Orzuev Sh., Ibragimov I., Alimova A., Weak gravitational lensing in SIS plasma with Gauss-Bonnet theory// "Fizika fanining rivojida iste'dodli yoshlarning o'rni" Respublika ilmiy-amaliy konferensiya (RIAK-XVII-2024) materiallari to'plami:O'zMU, 5-6-aprel, 2024-yil.Toshkent.31-32 betlar

11. Alibekov H., Alimova A., Khamidov V., Gravitational lensing and redshift of photons in the spacetime of deformed RN BH// "Fizika fanining rivojida iste'dodli yoshlarning o'rni" Respublika ilmiy-amaliy konferensiya (RIAK-XVII-2024) materiallari to'plami: O'zMU, 5-6-aprel, 2024-yil. Toshkent.47-48 betlar

Chapter I

Spinning particle motion around a black hole with quantum-corrected parameter

This chapter is about the motion of spinning particles around a quantum-corrected black hole. We investigate the dynamics of spinning test particles by using the Mathisson-Papapetrou-Dixon equations, the Tulczyjew spin-supplementary condition, and restricting the motion to the equatorial plane. We determine the innermost stable circular orbit (ISCO), effective potential, and effective force and examine how these depend on the black hole's α parameter and the particle's s spin. However, we also take into account a superluminal bound on the motion of the spinning particle since its kinematical four-velocity and dynamical four-momentum are not always parallel. We also show how the parameter α affects the maximum value of the spin parameter s. We determine the critical angular momentum of the particle for which a collision is possible by investigating collisions of spinning particles close to the horizon of a black hole.

1.1 Introduction

The black holes (BHs) are the most intriguing and fascinating objects in the Universe. The gravity of the BHs is dominating over all other interactions; thus, they play a role of cosmic laboratory for gravitational physics. General Relativity (GR) proposed by Einstein in 1915 properly describes the gravitational effects surrounding BH. Most of the existing experiments and observations are consistent with GR and adequately describe the effects around BH. Recent observation of the shadow of a supermassive BH [1,2] and detection of gravitational waves [3] can be considered as a test of GR in the strong-field regime. However, GR meets fundamental issues as a classical field theory. Particularly, the existence of singularity at the origin of classical solutions of GR and inconsistency with the quantum field theory require one to consider further modifications of GR or alternative theories of gravity. Fortunately, the current resolution of the experiments and observations used to test GR allows one to consider such modifications.

In the literature, there exist a large number of modified and alternative theories of gravity. In order to sort out these theories, one needs to develop corresponding tests of the particular theory. The huge number of theories creates an additional problem related to the degeneracy issues: the parameters of different theories/models may mimic each other. In order to resolve this issue, one needs to develop independent experimental/observational tests. Other ways of solving this problem can be performed by introducing the parameterization of the space-time metric [4–6].

No hair theorem claims that the solution of field equations describing BH may carry only three parameters: mass M, angular momentum J, and electric charge Q [7,8]. Possible modifications of GR may be related to the reconsideration of this theorem and include additional charges of BH, which may lead to the

quantum hair [9]. One of the possible quantum hair of BH is considered in Ref. [10] where the authors have found that trivial deformations of the seed Schwarzschild vacuum preserve the energy conditions and provide a new mechanism to evade the no-hair theorem. Other works devoted to the analysis of hairy BH can be found in [11, 12]. The motion of particles around compact gravitating objects may be used as a useful tool to test gravity theories. In metric theories of gravity, test particles follow the geodesics, and thus the trajectories of the particles may provide information about the physical parameters of the central object. On the other hand, particles with non-zero spin parameters will be deflected form geodesics due to interaction of spin and curvature of the spacetime. The exploration of the spinning particles motion may provide more information about spacetime structure. The dynamics of non-zero spin particles can be explored using MPD [13]. Mathisson-Papapetrou-Dixon (MPD) equations contain terms that are responsible for the interaction of the spin tensor and the curvature tensor. One of the main features of the spin-particle dynamics is spin precession [14–16]. We intend to investigate the dynamics of spinning particles in the vicinity of the quantum-corrected BH characterized by the solution presented in [17]. The chapter is structured as follows. We examine the solution of a quantum-corrected BH in Section 1.2. Section 1.2 is dedicated to the examination of the equations of motion for spinning particles in a generic context. The behavior of spinning particles around quantum-corrected BHs has been examined in Section 1.3. We summarize our findings in Section 1.4.

1.2 Basic equation of motion

Quantum corrected black hole

The classical BH solutions are altered by quantum corrections, which may cause variations in the behavior of nearby particles. By adding higher-order terms in the curvature to the Einstein-Hilbert action, the effective field theory approach introduces one such correction. We aim to examine the dynamics of spinning particles near the quantum-corrected black hole, described in spherical coordinates by the solution presented in [17, 18].

$$ds^2 = -f(r)dt^2 + f(r)^{-1}dr^2 + r^2 d\theta^2 + r^2 \sin^2\theta d\phi^2. \tag{1.1}$$

In the above equation $f(r)$ representing the lapse function, which is further defined as:

$$f(r) = 1 - \frac{2M}{r} + \frac{\alpha M^2}{r^4}, \tag{1.2}$$

where M represents the Arnowitt-Deser-Misner mass, and $\alpha = 16\sqrt{3}\pi\gamma^3 l_P^2$ is a parameter influenced by quantum corrections. In this expression, γ denotes the Immirzi parameter which measures the size of the quantum of area in Planck units while l_P refers to the Planck length [19]. Quantum corrections introduce a minimum mass M_{min} for the quantum corrected BH. This solution originates from the quantum extension of the Oppenheimer-Snyder model in the framework of Loop Quantum Cosmology. For simplicity, we use the dimensionless parameter $\hat{\alpha} = \alpha/M^2$ instead of α throughout this work. When $\hat{\alpha} = 0$, the Eq.(1.1) simplifies to the line element of a standard Schwarzschild BH. In order to investigate the parameter space that makes this space time be a black hole, we will study the horizon condition by requiring $f(r) = 0$ and $f'(r) = 0$. The extremal configuration, which provides the critical value $\hat{\alpha} = \frac{27}{16}$, is associated to the simultaneous

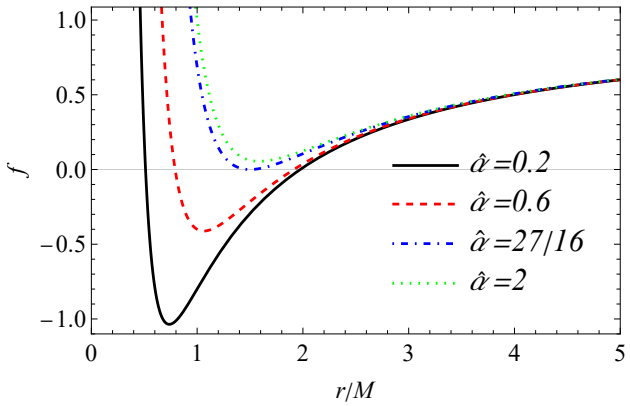

Figure 1.1: The radial dependence of the lapse function for different values of the parameter $\hat{\alpha}$.

solution. Black hole solutions thus exist for $\hat{\alpha} < \frac{27}{16}$. We can see from Fig.1.1 that for the values $\hat{\alpha} > \frac{27}{16}$ a horizonless configuration arises.

Equations of motion for a spinning particle

Spinning particles move in significantly different ways compared to non-spinning ones. While spinning particles follow differential equations with additional variables related to the connection between the Riemann curvature tensor and the particle's spin, non-spinning particles follow the geodesic equation within the specified background geometry. The set of differential equations for describing the motion of massive spinning particles is called the MPD equations [14,15] and has the following form:

$$\frac{Dp^{\alpha}}{d\lambda} = -\frac{1}{2}R^{\alpha}{}_{\beta\delta\sigma}u^{\beta}S^{\delta\sigma}, \quad \frac{DS^{\alpha\beta}}{d\lambda} = p^{\alpha}u^{\beta} - p^{\beta}u^{\alpha}, \tag{1.3}$$

where $D/d\lambda \equiv u^{\alpha}\nabla_{\alpha}$ is the projection of the covariant derivative along the trajectory of the particle as $u^{\mu} = dx^{\mu}/d\lambda$ is the test particle's 4-velocity, p^{α} is the canonical 4-momentum, $R^{\alpha}{}_{\beta\delta\sigma}$ is the Riemann curvature tensor, λ is an affine parameter and $S^{\alpha\beta}$ is the antisymmetric spin tensor: $S^{\alpha\beta} = -S^{\beta\alpha}$. Alternatively,

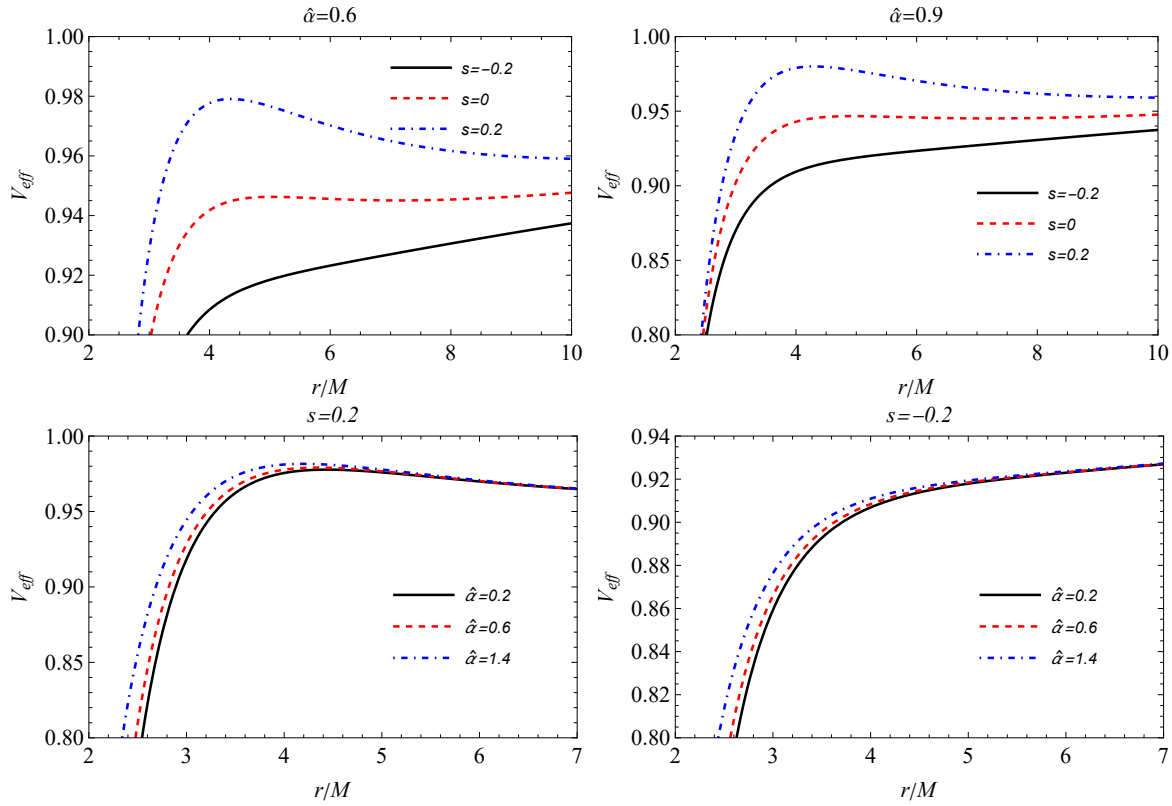

Figure 1.2: The radial dependence of the effective potential, V_{eff}, for varying parameter sets. The upper row illustrates the behavior of V_{eff} for fixed values of the parameter $\hat{\alpha} = 0.6$ and 0.9, with different spin values $s = -0.2, 0, 0.2$. The lower row highlights fixed spin values $s = -0.2$ and 0.2, while varying $\hat{\alpha} = 0.2, 0.6, 1.4$.

when the components of $S^{\mu\nu}$ are null, the differential equation simplifies as:

$$\frac{Dp^{\mu}}{d\tau} = 0. \tag{1.4}$$

The Mathisson–Papapetrou–Dixon equations require an additional spin supplementary condition (SSC) to uniquely fix the center-of-mass worldline of a spinning particle. The most commonly used SSCs are given by

$$\text{Pirani condition:} \qquad S^{\mu\nu}u_{\nu} = 0, \tag{1.5}$$

$$\text{Tulczyjew–Dixon condition:} \qquad S^{\mu\nu}p_{\nu} = 0, \tag{1.6}$$

$$\text{Newton–Wigner condition:} \qquad S^{\mu\nu}n_{\nu} = 0, \tag{1.7}$$

$$\text{Corinaldesi–Papapetrou condition:} \qquad S^{0i} = 0. \tag{1.8}$$

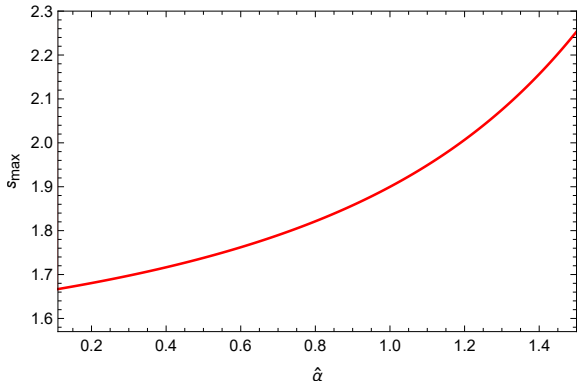

Figure 1.3: Maximal value of spin parameter dependence of $\hat{\alpha}$,

In the present work, we adopt the Tulczyjew–Dixon condition (1.6) due to its covariance and physical consistency.

The SSC relation and the MPD equations yield two independent conserved quantities: the canonical momentum and the particle's spin, as defined by the following relations:

$$\begin{aligned} S^{\alpha\beta}S_{\alpha\beta} &= 2S^2, \\ p^\alpha p_\alpha &= -m^2. \end{aligned} \tag{1.9}$$

Now, by using Eq. (1.3), one can introduce the following quantity

$$\mu = -p^\beta u_\beta. \tag{1.10}$$

Further, Eq. (1.3) gives the relation as:

$$p^\alpha = \mu u^\alpha - u^\beta \frac{DS^{\alpha\beta}}{D\lambda}. \tag{1.11}$$

The above expression indicates that the momentum and velocity vectors are no longer parallel for spinning particles.

Moreover, along with the SSC-dependent conserved values, there exist standard background-dependent conserved quantities linked to the Killing vectors. In an axially symmetric space-time, two Killing vector fields exist. One belongs to invariant time translations ξ^α, while the other allows rotations about the azimuthal

angle ϕ, ψ^α. These quantities can be calculated using the following equation:

$$p^\alpha \kappa_\alpha - \frac{1}{2} S^{\alpha\beta} \nabla_\beta \kappa_\alpha = p^\alpha \kappa_\alpha - \frac{1}{2} S^{\alpha\beta} \partial_\beta \kappa_\alpha = \text{constant}, \tag{1.12}$$

where k^α represents the two fields of the Killing vector: ξ^α and ψ^α.

Superluminal Bound

It is worth mentioning the fact that spinning particles should have a constraint for the values of spin, a superluminal constraint, above which the velocity of the particle exceeds the speed of light, which is non-physical.This is because the four-velocity u^α and the four-momentum p^α are not parallel. The four-velocity of the particle u^α is not time-like, but the four-momentum p^α is clearly a conserved quantity (see Eq.(1.9)) and always time-like. As a result, the normalization requirement $u^\alpha u_\alpha = -1$ is not sufficiently satisfied and the values of the normalization condition may be positive for certain spin values s. As a result, the particle's motion loses its physical significance and takes on the appearance of space-like.

The following restriction must be applied (on the equatorial plane) in order to maintain the trajectory of spinning test particles with a time-like character:

$$\frac{u_\alpha u^\alpha}{(u^t)^2} = g_{tt} + g_{rr}\dot{r}^2 + g_{\varphi\varphi}\dot{\varphi}^2 \leq 0. \tag{1.13}$$

In this case, the derivative with respect to the time coordinate t is indicated by the dot. The following form represents the expressions for dr/dt and $d\varphi/dt$ obtained by solving the MPD equations:

$$\begin{aligned} \frac{dr}{dt} &= \frac{u^r}{u^t} = \frac{\mathcal{C} p_r}{\mathcal{B} p_t}, \\ \frac{d\varphi}{dt} &= \frac{u^\varphi}{u^t} = \frac{\mathcal{A} p_\varphi}{\mathcal{B} p_t}, \end{aligned} \tag{1.14}$$

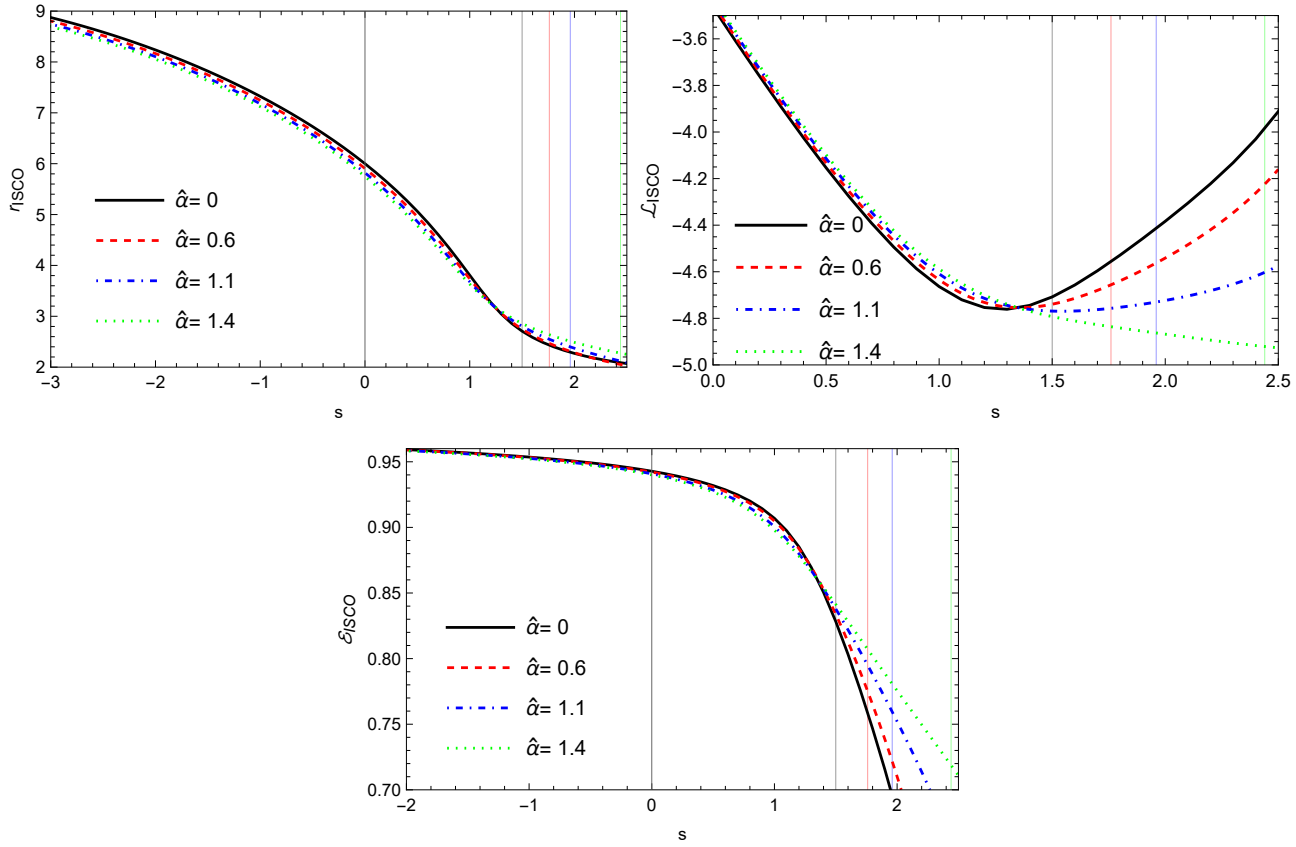

Figure 1.4: The variation of the radius, specific angular momentum, and energy at ISCO for fixed values of $\hat{\alpha}$ in spin parameter s .

where

$$\begin{aligned}\mathcal{A} &= g^{\varphi\varphi} + \left(\frac{S^{\varphi r}}{p_t}\right)^2 R_{trrt},\\ \mathcal{B} &= g^{tt} + \left(\frac{S^{\varphi r}}{p_t}\right)^2 R_{\varphi rr\varphi},\\ \mathcal{C} &= g^{rr} + \left(\frac{S^{\varphi r}}{p_t}\right)^2 R_{\varphi tt\varphi}.\end{aligned} \tag{1.15}$$

To determine the *superluminal bound*, we establish the function $\mathcal{F} = u_\alpha u^\alpha/(u^t)^2$ and investigate three cases:

- if $\mathcal{F} < 0$, the particle's journey is time-like and the spin values are physical.
- if $\mathcal{F} = 0$, there is a superluminal bound (the critical values of spin s_{max}).

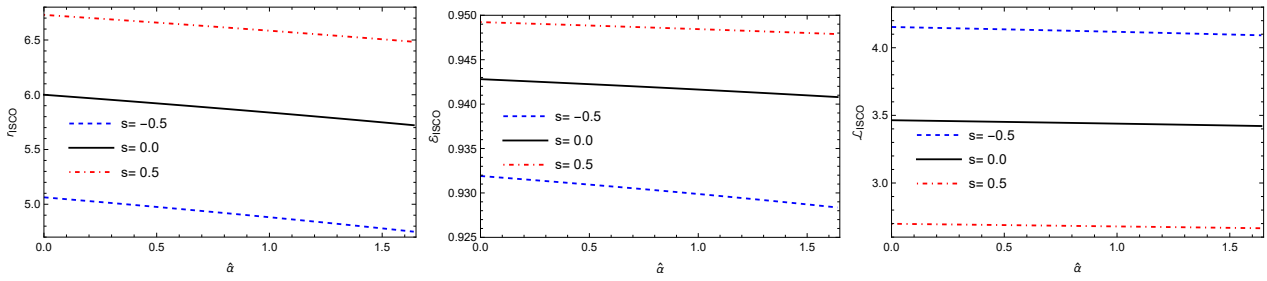

Figure 1.5: The variation of the radius, specific angular momentum, and energy at the ISCO with respect to the parameter $\hat{\alpha}$ of the BH for various particle spin values.

- if $\mathcal{F} > 0$, the spinning test particle follows a space-like trajectory with non-physical spin values (forbidden).

To put it simply, the superluminal bound is the threshold that distinguishes space-like trajectories from time-like ones. The spin values of the test particle are valid until the function vanishes $\mathcal{F} = 0$. This is because, according to condition Eq.(1.13), positive values of $\mathcal{F}$ indicate that the test particle may have a velocity that exceeds the speed of light c, which is non-physical. The second condition mentioned above yields the critical values of the spin s_{max}.

1.3 Dynamics of spinning particles around quantum corrected black hole

The effective potential

In the preceding section, we examined the fundamental principles of the equations that describe the motion of a spinning particle. This section focuses on the analysis of spinning particle dynamics within the specified metric (Eq.(1.1)).

Initially, our objective was to determine the effective potential of a rotating test particle in the vicinity of a quantum-corrected BH. In order to simplify the

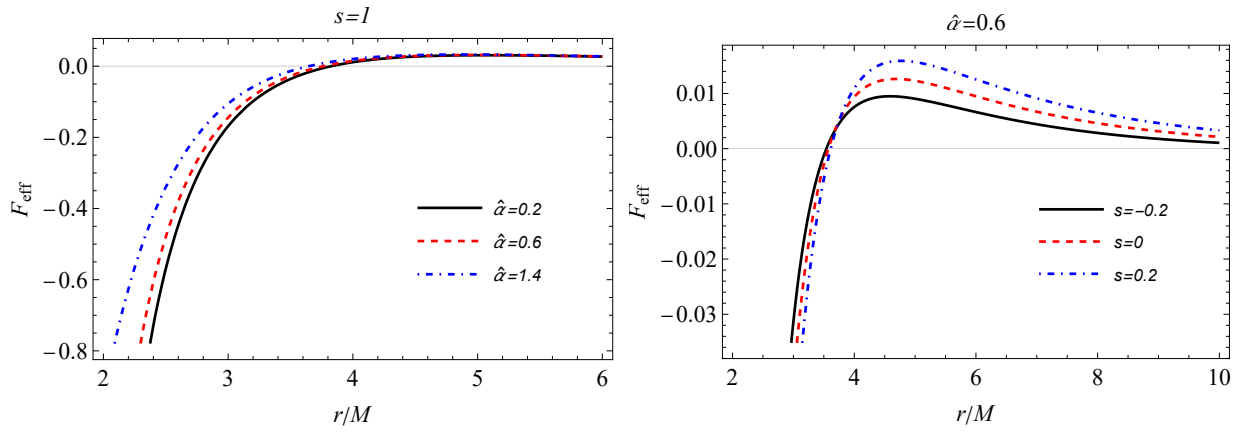

Figure 1.6: Effective force as a function of radial distance in various spin parameter s and $\hat{\alpha}$.

equation, we examine the motion within the equatorial plane ($\theta = \pi/2$).

In static and spherically symmetric spacetimes, there exist two conserved quantities: energy E and total angular momentum J (where $J = L + S$), with S representing spin and L representing orbital angular momentum. Further, both quantities are defined as:

$$\begin{aligned} -E &= p_t - \frac{1}{2} g_{tt,r} S^{tr} \\ J &= p_\phi - \frac{1}{2} g_{\phi\phi,r} S^{\varphi r}, \end{aligned} \tag{1.16}$$

Furthermore, considering the motion of the particle is constrained to the equatorial plane, the antisymmetric spin tensor $S^{\alpha\beta}$ has just two independent components [20] which are expressed as:

$$\begin{aligned} S^{tr} &= \frac{p_\phi s}{\sqrt{-g_{tt} g_{rr} g_{\phi\phi}}}, \\ S^{\varphi r} &= -\frac{p_t s}{\sqrt{-g_{tt} g_{rr} g_{\phi\phi}}}, \end{aligned} \tag{1.17}$$

where, $s = S/m$ represents the specific spin angular momentum of the particle, which can be positive or negative depending on the direction of p_ϕ. Substituting Eq. (1.17) into Eq. (1.16) and performing basic calculations, the formulations for

energy E and total angular momentum J can be reformulated as:

$$\begin{aligned} -E &= p_t - \frac{s p_\phi g_{tt,r}}{2\sqrt{-g_{tt} g_{rr} g_{\phi\phi}}} = p_t + \frac{s}{2r} f'(r) p_\phi \\ J &= p_\phi + \frac{s p_t g_{\phi\phi,r}}{2\sqrt{-g_{tt} g_{rr} g_{\phi\phi}}} = p_\phi + s p_t. \end{aligned} \tag{1.18}$$

By solving the above system for p_t and p_ϕ, one can easily get the following results:

$$\begin{aligned} p_t &= \frac{\mathcal{J} M s \left(2\alpha M - r^3\right) - E r^6}{2\alpha M^2 s^2 - M r^3 s^2 + r^6}, \\ p_\phi &= \frac{r^6 (E s + \mathcal{J})}{2\alpha M^2 s^2 - M r^3 s^2 + r^6}. \end{aligned} \tag{1.19}$$

Now, from Eq. (1.9), one can get the expression for the radial canonical momentum as:

$$(p^r)^2 = -g^{rr}[g^{tt} p_t^2 + g^{\phi\phi} p_\phi^2 + m^2]. \tag{1.20}$$

By substituting Eq. (1.19) and the components of the metric tensor into Eq. (1.20), one can easily derive the quadratic equation for the energy E of the spinning particle [20, 21] as:

$$\rho (u^r)^2 = \alpha \mathcal{E}^2 + \delta \mathcal{E} + \gamma, \tag{1.21}$$

where,

$$\alpha = 4[r^2 - s^2 f(r)], \tag{1.22}$$

$$\delta = 4 s \mathcal{J} [-2 f(r) + f'(r) r], \tag{1.23}$$

$$\gamma = \mathcal{J}^2 \left[f'(r)^2 s^2 - 4 f(r)\right] - f(r) \left[2r - f'(r) s^2\right]^2 \tag{1.24}$$

$$\rho = \left[2r - f'(r) s^2\right]^2. \tag{1.25}$$

Now, in further calculations, one can use the following dimensionless variables: $\mathcal{J} = \frac{J}{mM}$, $s = \frac{\mathcal{S}}{mM}$, $\mathcal{E} = \frac{E}{mM}$. Now, one can rewrite Eq. (1.21) as:

$$(u^r)^2 = \frac{\alpha}{\rho} (\mathcal{E} - V_+)(\mathcal{E} - V_-) \ . \tag{1.26}$$

To achieve the circular motion of the spinning particles, we impose the condition $u^r = 0$, from which we can define the effective potential [22, 23] in the following manner:

$$V_{\pm} = \frac{-\delta \pm \sqrt{\delta^2 - 4\alpha\gamma}}{2\alpha} \ . \tag{1.27}$$

One can define the effective potential under the following assumption that spinning particles possess positive energy: $V_{eff} = E_+$. Fig. 1.2 demonstrates the radial dependence of the effective potential at fixed $\mathcal{L} = 3.5$ for different values of the parameter $\hat{\alpha}$ and s. The upper row of the plot shows the dependence of the effective potential on the radial motion of the spinning particle for different values of s, with the parameter fixed at $\hat{\alpha} = 0.6$ and $\hat{\alpha} = 0.9$. An increase in the parameter $\hat{\alpha}$ results in an increase in the effective potential. In contrast, the bottom row of the plot depicts the influence of the various values of the parameter $\hat{\alpha}$ on the effective potential at a fixed value $s = 0.2$ and $s = -0.2$. As r/M increases, V_{eff} approaches an asymptotic value, indicating stable behavior at large radial distances. We can see from the graph that, if s increase V_{eff} is also increases significantly. The bottom graphs show that for different values of the parameter $\hat{\alpha}$, V_{eff} is nearly similar at large radial distances.

Innermost stable circular orbit

We now examine the dynamics of a spinning particle in spacetime (1.1) by identifying the stable circular orbits, which are consistently the focal point of attention. It is widely recognized that two conditions must be satisfied for circular orbits:

(i) $dr/d\tau = 0$ or $\mathcal{E} = V_{eff}(r)$ (the motion with a constant radius R) and (ii) $d^2r/d\tau^2 = 0$ or $V'_{eff}(r) = 0$ (the motion with zero acceleration). However, these constraints alone do not ensure the stability of circular orbits. To guarantee

stability, the second radial derivative of the effective potential must be positive, specifically $d^2V_{eff}/dr^2 \geq 0$. Moreover, the equality of the last condition signifies the ISCO. So, the dependence of the ISCO radius, the specific angular momentum, and the specific energy at ISCO on the spin s for different values of $\hat{\alpha}$, is presented in Fig. 1.4.The graphs indicate that for small values of the spin parameter s, an increase in the parameter $\hat{\alpha}$ leads to a decrease in the ISCO radius $r_{\rm ISCO}$, the specific energy $\mathcal{E}_{\rm ISCO}$, and the specific angular momentum $L_{\rm ISCO}$. Beyond a certain value of s, the curves for larger values of $\hat{\alpha}$ cross over and switch positions with those for smaller $\hat{\alpha}$. This suggests a complex interaction between $\hat{\alpha}$ and s, possibly due to dynamic changes in orbital stability and spacetime geometry at high spin. Moreover, the third graph of the specific energy is of particular interest. As observed, the ISCO energy is independent of the parameter $\hat{\alpha}$ to $s \approx 1.5$ and begins to differ noticeably only after $s \approx 1.5$. Additionally, the vertical lines in Fig. 1.4 define *the superluminal bound*, the maximum values of the spin s, after which the values of the ISCO are non-physical. In other words, the left side of the lines corresponds to the time-like particles, while the right side represents space-like particles, which lacks physical meaning. Furthermore, the influence of the same physical quantities ($r_{\mathcal{ISCO}}$, $\mathcal{L}_{\mathcal{ISCO}}$), and $\mathcal{E}_{\mathcal{ISCO}}$ on the parameter α for different spin s values is illustrated in Fig. 1.5. The plot illustrates a linear relationship between $r_{\mathcal{ISCO}}$ and $\mathcal{E}_{\mathcal{ISCO}}$ with respect to $\hat{\alpha}$, and a rise in spin s results in higher function values. The dependence of the particle's angular momentum $\mathcal{L}_{\mathcal{ISCO}}$ on $\hat{\alpha}$ remains largely unaffected. In Fig. 1.3, the variation of the critical spin values s_{max} with respect to $\hat{\alpha}$ is presented. Clearly, when the $\hat{\alpha}$ parameter increases, the critical value of the spin also increases.

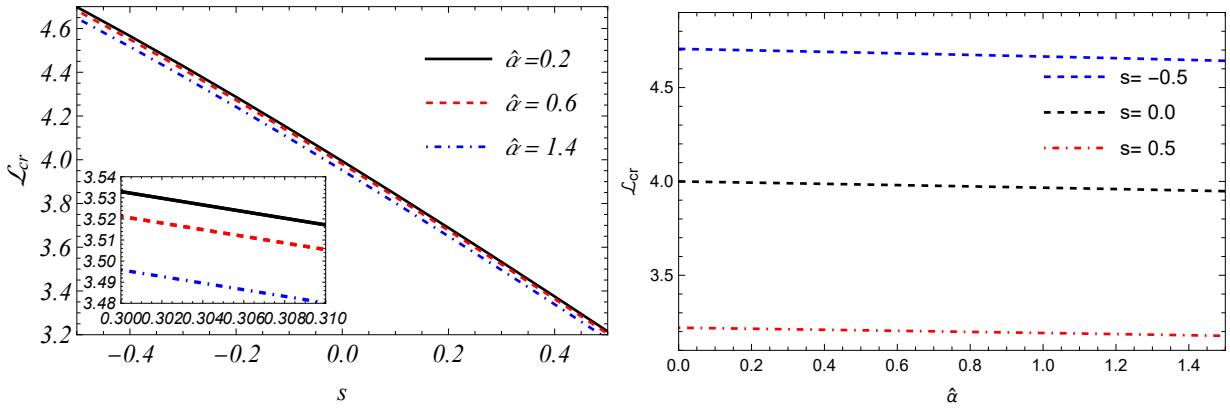

Figure 1.7: Dependence of critical angular momentum on the spin s and $\hat{\alpha}$.

Effective force

The effective force acting on a particle reveals its motion, indicating whether it is being attracted toward the BH or moving away from it. We examine the spinning particle's motion around quantum-corrected BH, where both attractive and repulsive gravitational forces can occur. Using the expression for V_{eff}, we determine the effective force acting on the particles, which is given by

$$F = -\frac{1}{2}\frac{dV_{eff}}{dr}. \tag{1.28}$$

The behavior of the effective force around the quantum-corrected BH is shown in Fig. 1.6, as a function of r, for the parameter of varying values of $\hat{\alpha}$ and spin s. It is noted that the effective force acting on the particles has the same behavior for both the parameters $\hat{\alpha}$ and the parameters s. The effective force is small when the parameter $\hat{\alpha}$ or the spin parameter s has small values, however, the effective force increases when the parameter $\hat{\alpha}$ or s increases. When we fix s and vary $\hat{\alpha}$, the effective force radial profiles coincide as the radial distance r increases. However, for varying values of $\hat{\alpha}$, different radial profiles of the effective force can be observed as the radial distance r increases.

1.4 Conclusion

This chapter is devoted to investigating the spinning particle motion around a quantum-corrected BH. Initially, we have examined the fundamental principles of spinning particle motion using the MPD equations. The effective potential V_{eff} of the spinning particle has been computed and its radial dependency has been graphed for various parameter values of $\hat{\alpha}$ and s. Consequently, both parameters increase the effective potential.

Furthermore, the influence of parameters $\hat{\alpha}$ and spin s on the ISCO has been examined. The presence of the parameter $\hat{\alpha}$ reduces the radius of the ISCO. The influence of the same parameters on the angular momentum and energy at ISCO has been observed. The presence and variation of the parameter $\hat{\alpha}$ increase the specific angular momentum while diminishing the energy at the ISCO up to the joining point.

Moreover, constraints on spin s (the *superluminal bound condition*) have been identified, beyond which the particle's trajectory becomes space-like and non-physical. The relationship between the critical values of spin s_{max} and $\hat{\alpha}$ has been illustrated and analyzed. We have also analyzed the effective force surrounding the quantum-corrected BHs as a function of r, for different values of the parameters $\hat{\alpha}$ and s. The effective force acting on the particles exhibits a similar trend for both the parameter $\hat{\alpha}$ and the spin parameter s. Specifically, the effective force is minimal when $\hat{\alpha}$ or s is small but increases as these parameters grow. When the parameter s is maintained constant and the BH parameter $\hat{\alpha}$ is varied, the radial profiles of the effective force converge as the radial distance r increases. However, for different values of s, distinct radial profiles of the effective force can be observed as the radial distance r increases.

Chapter II

Optical properties of Reissner-Nordström-like black hole in the presence of plasma

In this chapter, we investigate weak gravitational lensing and shadow radius in the Kalb-Ramond (KR) gravity for an Reissner-Nordstrom-like (RN-like) black hole (BH). The examination is carried out in three distinct frameworks: uniform plasma, singular isothermal sphere(SIS), and non-singular isothermal sphere (NSIS). When a gravitating object is surrounded by plasma, the lensing angle is determined by the frequency of the electromagnetic wave, plasma dispersion, plasma inhomogeneity, and gravity. Even in uniform plasma, the gravitational photon deflection angle differs from that in a vacuum and depends on photon frequency due to the second effect. We consider both effects and calculate the lensing angle for a significantly non-uniform plasma in the existence of KR gravity. Utilizing observational data from the Event Horizon Telescope (EHT) project for Sgr A*, we have obtained that which range of RN-like black hole's parameters Q and l correspond observations as well as when the Lorentz-violating parameter l rise, radius of black hole shadow decrease. To connect a relationship with observations

data, we examine the magnification and positioning of images produced by lensing, as well as the weak deflection angle and magnification for sources located near various galaxies.

2.1 Introduction

Black holes are areas in which gravity is so intense that nothing can escape from them, not even light. Since they cast doubt on our perceptions of gravity, space, and time, they are essential to our comprehension of basic physics. Investigating black holes helps us understand the universe's extreme conditions, learn more about the structure of spacetime, and advance theories like quantum field theory and general relativity. It is also worth to note that black holes are believed also essential in forming galaxies and the Universe's evolution. General Relativity (GR) proposed by Albert Einstein is the main theory describing the black hole physics. Within GR there are a number of different black hole solutions describing stationary charged (Reissner-Nordstrom), rotating charged (Kerr-Newman), rotating uncharged (Kerr), and stationary uncharged (Schwarzschild) black holes. Recent observations and experiments justified with high accuracy that the objects M87 and Sgr A* are mostly likely spinning black holes [24–26].

GR is well tested theory describing the gravity using the geometrical approach. The first observational test of the GR based on the gravitational lensing has been provided by Arthur Eddington during the Solar eclipse observation in 1919 [27]. The gravitational lensing is one of the fundamental features of the metric theory of gravity including GR. Later GR has been successfully tested in weak and strong field regimes (see, e.g. [28, 29]). On the other hand, there is a need for modified and alternative theories of gravity due to the presence of fundamental problems of GR related to singularity issue, noncompatibility with quantum field

theory, etc. There is belief that quantum gravity theory will resolve this issues, and modified and alternative gravity theories are step forward in discovering this theory. However, any modifications or alternates to GR has to be tested. The current resolutions of the experiments and observations allows to construct tests and get corresponding constraints on corresponding parameters of the model [30–33].

One of the modifications of GR is possible due to introducing additional vector and or scalar fields. In addition to a vector field, the possibility of using a rank two antisymmetric tensor field known as the Kalb-Ramond (KR) field has been explored as a potential source for Lorentz symmetry breaking (LSB) [34]. The KR field arises in the spectrum of bosonic string theory [35], and its characteristics have been thoroughly examined in different domains, including black hole physics [36, 37], cosmology [38], and the braneworld scenario [39, 40]. When the KR field forms a nonminimal coupling with gravity and obtains a non-zero vacuum expectation value (VEV), the Lorentz symmetry undergoes spontaneous breaking. Lessa et al. proposed a precise and spherically symmetric solution under the background of the vacuum expectation value (VEV) of the Kaluza-Klein (KR) field [41]. Astrophysical processes around the black hole in KR gravity have been studied in Refs. [42, 43].

As already mentioned, gravitational lensing was among the initial investigations of GR [44]. The phenomenon was initially identified through the Sun's deflection of light, followed by the lensing of quasars by galaxies in the foreground. Subsequently, it was observed in the creation of large arcs in galaxy clusters and in galactic microlensing. Currently, it is a common occurrence in the field of astronomical observations (see to [45] for a comprehensive analysis and relevant sources).

Synge presents a comprehensive theory of geometrical optics in curved space-

time, applicable to any medium [46]. Bisnovatyi-Kogan and Tsupko have created the model of gravitational lensing in plasma based on his general approach. They demonstrated that a novel effect emerges in a nonlinear framework [47]. Even in a uniform plasma, the gravitational deflection angle is contingent upon the frequency of the photon and differs from the scenario in a vacuum.

In this chapter, we explore the deflection angle of a photon traveling through a weak gravitational field around charged black hole in KR gravity within an arbitrary inhomogeneous plasma and black hole shadow is studied with comparing observational data. In Sect. 2.2, we give a brief review of RN-like black hole in Kalb-Ramond gravity as well as null geodesic equations in RN-like black holes in the Kalb-Ramond spacetime. In Sect. 2.3, we examine the RN-like black hole in Kalb-Ramond metric with shadow of the black hole, In Sect. 2.4, we estimate an angle of the deflection and a magnification in the weak field limit in a plasma. Finally, in Sect. 2.5, we summarize the obtained results.

2.2 Particle dynamics

In Boyer-Lindquist coordinates, the RN-like BH metric is given by [48, 49]

$$ds^2 = -f(r)dt^2 + f(r)^{-1}dr^2 + r^2(d\theta^2 + \sin^2\theta d\phi^2), \tag{2.1}$$

with

$$f(r) = \frac{1}{1-l} - \frac{2M}{r} + \frac{Q^2}{(1-l)^2 r^2}, \tag{2.2}$$

where l is a dimensionless Lorentz-violating parameter [48]. By using Eq.(2.2) we can find the radius of the BH horizon as

$$r_h = (1-l)(M \pm \sqrt{M^2 - \frac{Q^2}{(1-l)^3}}). \tag{2.3}$$

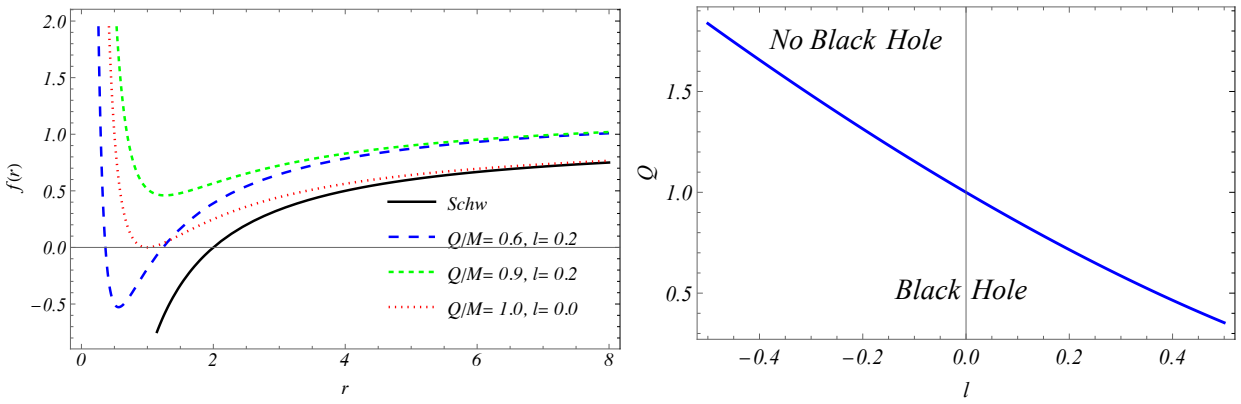

Figure 2.1: This graph shows a variation of $f(r)$ (left-hand side) and event horizon radius due to the RN-like BH in the KR gravity and region (right-hand side), where a black hole can exist or not

According to (2.3), BH's horizon could be narrower than Schwarzschild's in the presence of a Kalb-Ramond field. It is obvious that the $l < 1$ requirement needs to be met at all times. Furthermore, when $l \to 0$, this measure simplifies to the Schwarzschild metric. The left panel of Fig. 2.1 illustrates the radial dependency of $f(r)$ and the relationship between the event horizon radius and both the total charge of the black hole and the l parameter. Given the values of Q and l, it is possible to see either one, two, or no event horizon. Additionally, the range of Reissner-Nordstorm-like black holes for the parameters Q/M and l may be determined, as shown in Fig. 2.1. Using a Reissner-Nordstrm-like spacetime, we have established the presence of black holes and derived the relationship between the boundary separating them and the charge-to-mass ratio Q/M and l parameters. Referring to Fig. 2.1. (right side panel) Obtaining the value of the l parameter is likewise straightforward. The parameter l can range in value from $0.5 > l > -0.5$ as we obtain the black hole's charge, $Q/M > 0.3$.

Null geodesic in spacetime

As a photon propagates through a plasma medium, the Hamiltonian is given as [50]

$$H(x^{\alpha}, p_{\alpha}) = \frac{1}{2}\tilde{g}^{\alpha\beta}p_{\alpha}p_{\beta}. \tag{2.4}$$

In this context, x^{α} denotes spacetime coordinates, and $\tilde{g}_{\alpha\beta}$ stands for the effective metric, which can be expressed in a particular mathematical format as

$$\tilde{g}^{\alpha\beta} = g^{\alpha\beta} - (n^2 - 1)u^{\alpha}u^{\beta}, \tag{2.5}$$

The variables n, p_{α}, and u^{β} represent the refractive index of the plasma, the four-momentum of the photon, and the four-velocity of the photon, respectively. The plasma refractive index, denoted as n, is [51]

$$n^2 = 1 - \frac{\omega_p(r)^2}{\omega(r)^2}, \tag{2.6}$$

where $\omega_p^2(r) = 4\pi e^2 N(r)/m_e$ (e and m_e are the electron charge and mass, respectively, and N is the electron number density) is the electron frequency in the plasma, and the gravitational red-shift formula is used to calculate the photon frequency $\omega(r)$ as measured by a static observer

$$\omega(r) = \frac{\omega_0}{\sqrt{f(r)}}. \tag{2.7}$$

At infinity, $\omega_0 = \text{const}$ is the frequency ($f(\infty) = 1$) and $\omega_0 = \omega(\infty) = -p_t$, which denote the energy of the photon at spatial infinity [52]. Light can only travel through plasma if its frequency exceeds the plasma frequency. Therefore, Equation (2.6) is applicable only when the ratio of the plasma frequency to the light frequency is less than 1. If this ratio is more than 1, the photon cannot propagate through the plasma medium. If the frequency ω_0 is approximately equal to ω, then the deflection angle is significantly greater than in the vacuum situation where $\omega_p = 0$.

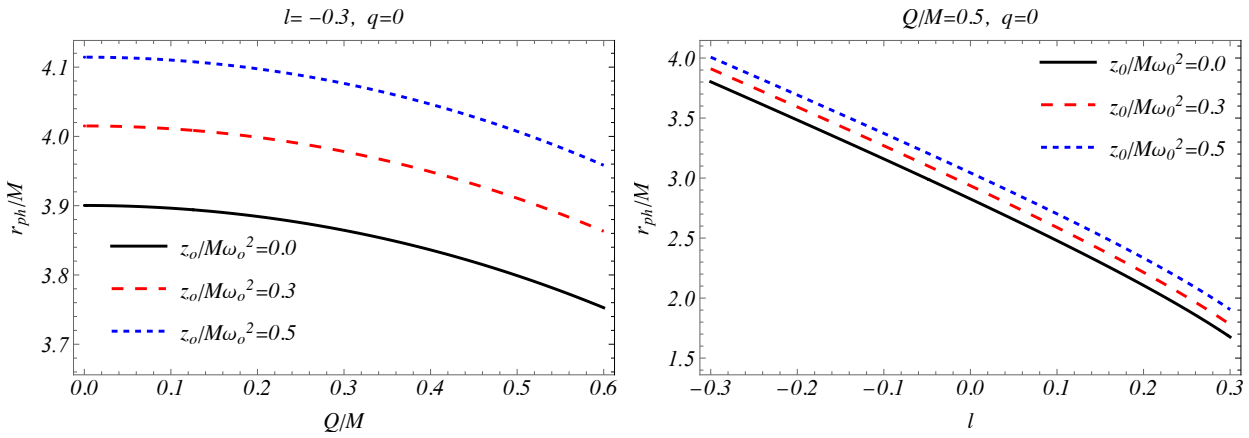

Figure 2.2: Plots of photon sphere as a function of black hole charge Q (left panel) and l parameter (right panel) in the case of $\omega_0^2/\omega^2 = const$.

The equation used to determine the radius of a circular orbit of light around a black hole, known as the photon sphere, is given by [52]

$$\frac{\mathrm{d}(\gamma^2(r))}{\mathrm{d}r}\Big|_{r=r_{ph}} = 0, \tag{2.8}$$

where

$$\gamma^2(r) \equiv r^2\left[\frac{1}{f(r)} - \frac{\omega_p^2(r)}{\omega_0^2}\right]. \tag{2.9}$$

The roots of Eq. 2.8 are not solvable analytically for most variations of $\omega_p(r)$. However, a few simplified sequences will be presented below.

Homegeneous plasma

For a homogeneous plasma, in the exceptional case where the plasma $\omega_p^2(r) = const$ frequency is constant throughout the medium. After solving Eq. (2.8) numerically, the result presented in Fig. 2.2. The black hole's charge makes it more difficult for photons to escape, bringing the photon sphere closer to the black hole, while the plasma environment changes the refractive index of light, causing the photon sphere to expand.

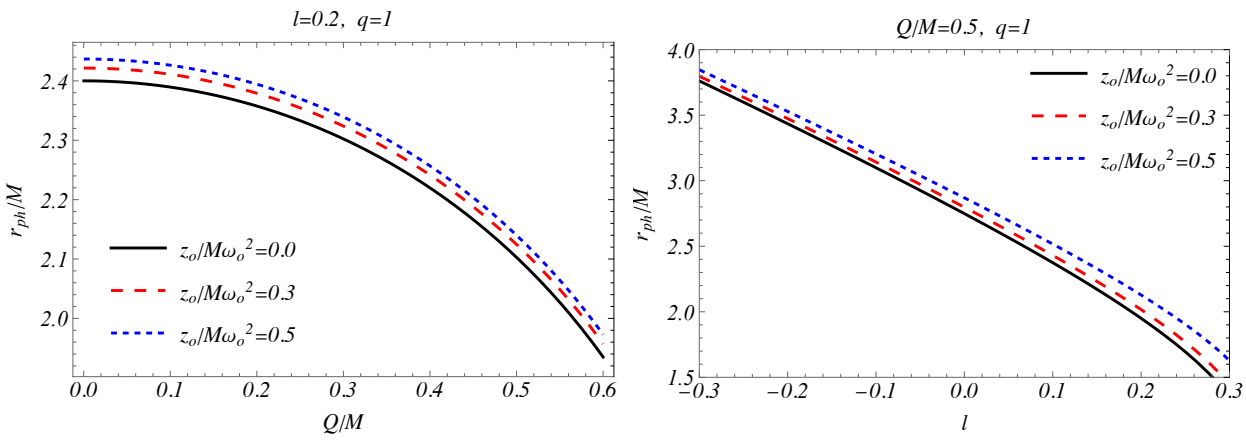

Figure 2.3: This figures illustrate radius of photon sphere with respect to Q/M and l parameters as a fixed $q = 1$ in-homogeneous case .

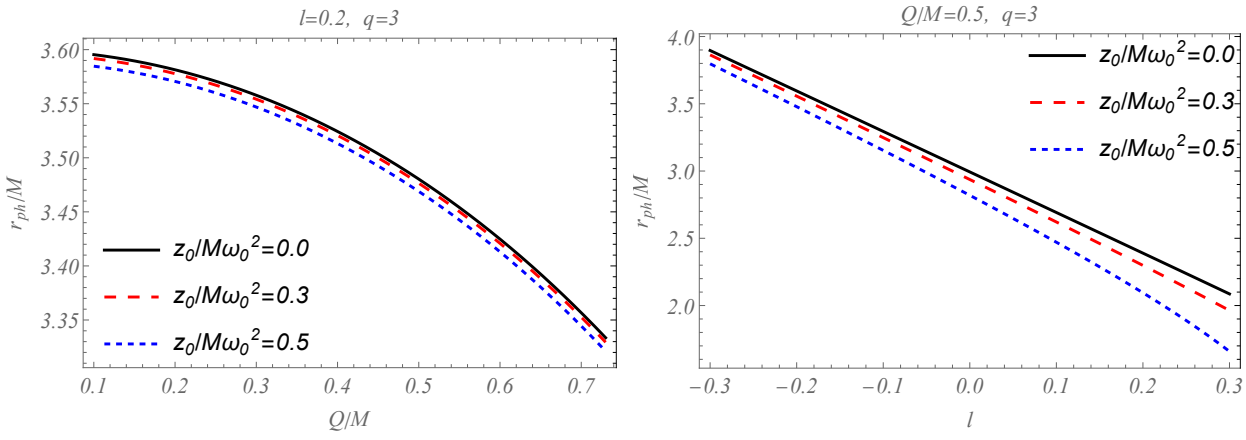

Figure 2.4: These figures give information about radius of photon sphere as a function of Q/M (left panel) and l (right panel) parameters with a $q = 3$ inhomogenous plasma medium.

Inhomogeneous plasma

Our current research involves the analysis of photon spheres in an inhomogeneous plasma, where the plasma frequency needs to follow a straightforward power-law relationship.

$$\omega_p^2(r) = \frac{z_0}{r^q}, \tag{2.10}$$

where z_0 is the free parameter. We limit our analysis to the following examples in order to examine the main characteristics of the power law model: $q = 3$ and z_0 as a constant that is connected to the stellar surface based on Goldreich-Julian (GJ) density, and $q = 1$ and z_0 as a constant that precisely reproduces the negative-mass divergent lens. After putting Eq. (2.10) into Eq. (2.8), We get numerical expression for the radius of the photon sphere in the inhomogeneous plasma medium, as plotted in Fig. 2.3 and Fig. 2.4. It is noticeable that increasing values of both Q/M and l parameters lead to a decrease in the radius of photon sphere. On the other hand, if $\omega_p^2(r) = z_0/r$ describes the distribution of the photon sphere, then the photon sphere radius rises due to the plasma medium($q = 1$), and decreases slightly when there is inhomogeneous plasma($q = 3$) surrounding the black hole. Furthermore, it is difficult to distinguish the difference in the effect on the photon radius between nonuniform and uniform plasma mediums. It implies that testing and differentiating between homogeneous and inhomogeneous plasma using the shadows of black holes will be difficult.

2.3 Shadow of a black hole surrounded by plasma medium

The radius of the RN-like space-time metric's shadow in the presence of both a uniform and a non-uniform plasma medium is examined in this section. An

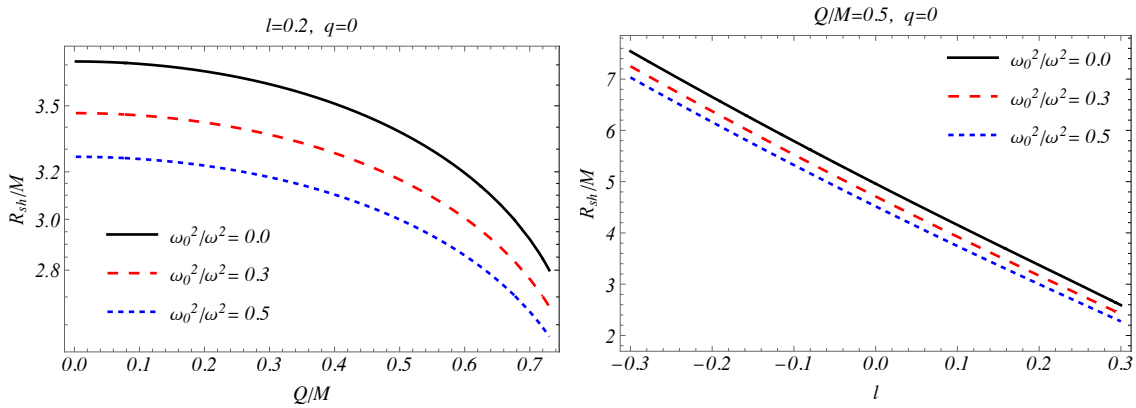

Figure 2.5: This graph illustrates variation of the radius of shadow R_{sh}/M concerning Q/M and l for the case $\omega_p^2 = z_0/r$.

geometry-based technique yields the angular radius α_{sh} of the black hole shadow [52, 53].

$$\sin^2 \alpha_{sh} = \frac{\gamma^2(r_p)}{\gamma^2(r_0)}, \tag{2.11}$$

The observer's position and the photon sphere's radius are denoted by the variables r_0 and r_p, respectively. By positioning the observer at a significant distance from the black hole, we can get an approximation formula for the radius of the black hole's shadow [52]

$$R_{sh} \approx r_0 \sin \alpha_{sh} = \sqrt{r_p^2 \left[\frac{1}{f(r_p)} - \frac{\omega_p^2(r_p)}{\omega_0^2} \right]}. \tag{2.12}$$

This is predicated on the fact that, for both plasma models, $l(r) \to r$, which is derived from Eq. (2.9) at spatial infinity. When $r_p = 3M$, we recover the radius of the Schwarzshild black hole shadow, $R_{sh} = 3\sqrt{3}M$, for vacuum $\omega(r) \equiv 0$.

In Fig. 2.5, the radius of the black hole shadow enclosing a homogeneous plasma is shown for various parameters Q/M and l. The shadow radius decreases more rapidly as the parameters Q/M and l increase, highlighting the dominant role of these quantities in shaping the shadow size. Furthermore, we have investigated

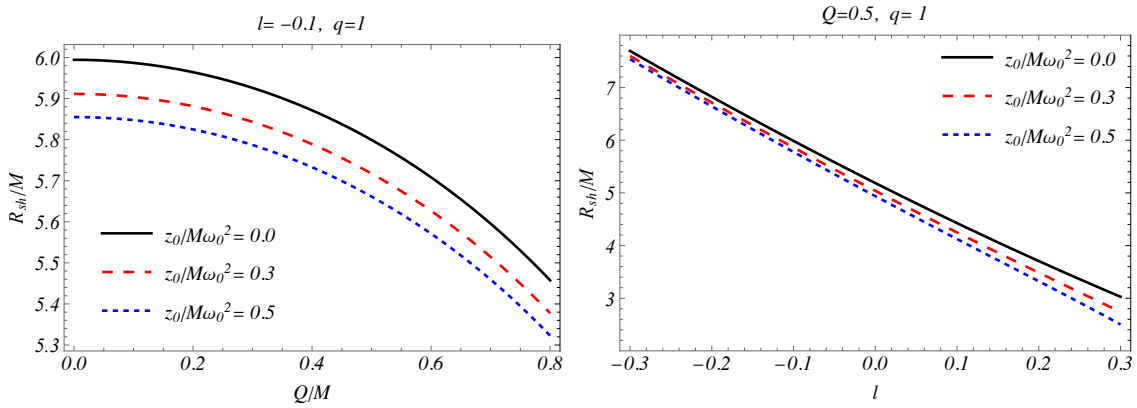

Figure 2.6: This graph illustrates variation of the radius of shadow R_{sh}/M concerning Q/M and l (bottom panel)for the case $\omega_p^2 = z_0/r$.

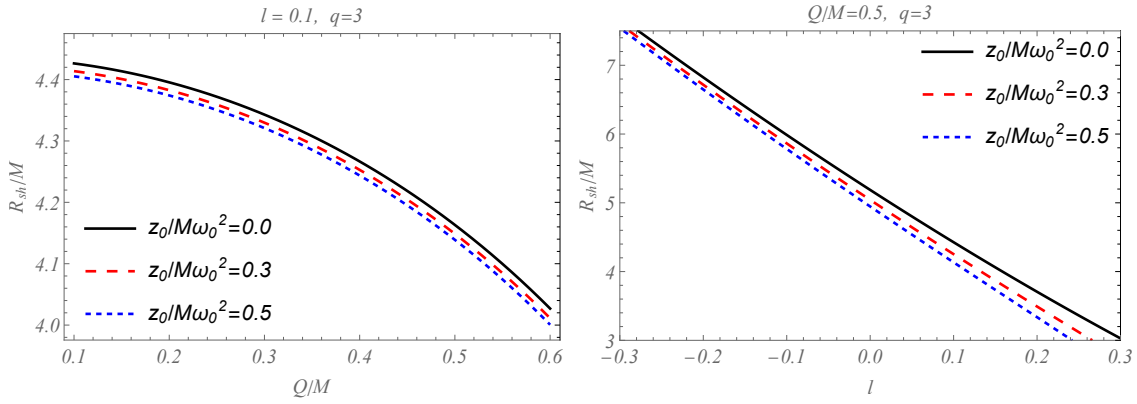

Figure 2.7: This graph illustrates variation of the radius of shadow R_{sh}/M concerning Q/M and l for the case $\omega_p^2 = z_0/r^3$.

inhomogeneous plasma with $\omega_p^2(r) = z_0/r^q$ (q=0,1,3) in Eq. (2.12). From Figs. 2.5-2.7 It is evident that the presence of plasma leads to a reduction in the black hole's shadow radius.

Constraints on black hole shadow

Now, we get constraints on BH shadow as done in [54]. We use the following 1σ and 2σ constraints on R_{sh}/M [55].

$$1\sigma : 4.55 \lesssim R_{sh} \lesssim 5.22, \tag{2.13}$$

$$2\sigma : 4.21 \lesssim R_{sh} \lesssim 5.56, \tag{2.14}$$

These constraints are motivated by an observation for Sgr A*s shadow which was reported in Ref. [56]. Although Sgr A* are known to be spinning black holes, the use of a static spherically symmetric metric in some EHT-based analyses is justified as a simplifying approximation. Non-rotating metrics allow for analytical tractability and enable the isolation of specific gravitational effects, such as deviations from General Relativity or the influence of additional parameters, without the added complexity of spin. Moreover, the shadow radius is only weakly sensitive to moderate rotation, while spin mainly affects the shadow shape. Therefore, static metrics remain useful for initial constraints and theoretical tests, despite the availability of more realistic Kerr-based simulations. The changes in the shadow radius depending on the electric charge Q of the object and Lorentz-violating parameter l are plotted in Fig. 2.8, illustrating the effects of the both uniform plasma (top panel)and non-uniform plasma(bottom panel) on RN-like black hole's spacetime. These plots agree well with observational data from the Event Horizon Telescope image of Sgr A* Eqs. (2.13) and (2.14). We can witness that a increasing value of l parameter leads the radius of BH's shadow to decrease. This phenomenon can

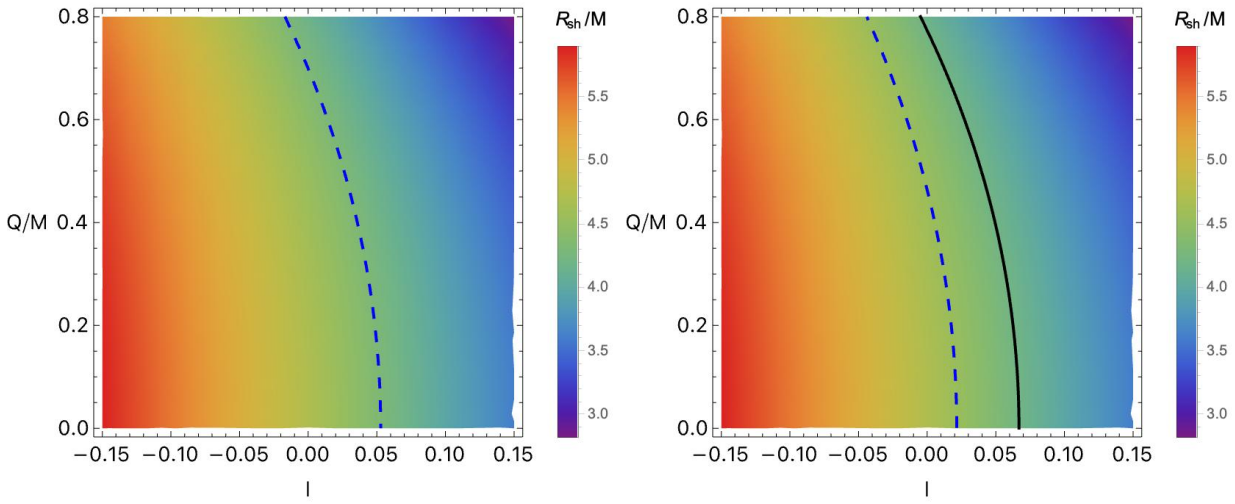

Figure 2.8: Constraint on the BH charge Q/M and the l parameters with uniform plasma $\omega_o^2/\omega^2 = 0.5$(left) and nonuniform plasma (right). The dashed and solid lines correspond to the minimum boundaries of 1σ and 2σ respectively.

be understood by examining how the charge of the BH influences BH's shadow experienced by test particles.

2.4 Weak gravitational lensing in Reissner-Nordström-like Kalb-Ramond spacetime with nonzero Lorentz violating parameter

This section focuses on investigating the impacts of gravitational lensing in the RN black hole within the context of gravity with a background KR field. We will be using a weak-field approximation, which is described as follows [57]

$$g_{\alpha\beta} = \eta_{\alpha\beta} + h_{\alpha\beta}, \tag{2.15}$$

where the Minkowski metric and perturbation metric, respectively, and their features are denoted by the symbols $\eta_{\alpha\beta}$ and $h_{\alpha\beta}$ [57]

$$\eta_{\alpha\beta} = diag(-1, 1, 1, 1), \tag{2.16}$$

$$h_{\alpha\beta} << 1, \quad h_{\alpha\beta} \to 0 \quad \text{under} \quad \mathrm{x}^{\alpha} \to \infty \tag{2.17}$$

$$g^{\alpha\beta} = \eta^{\alpha\beta} - h^{\alpha\beta}, \;\; h^{\alpha\beta} = h_{\alpha\beta}. \tag{2.18}$$

The deflection angle of the light trace might be expressed as [57]

$$\hat{\alpha}_b = \pm \int_0^{\infty} \Big[\frac{b}{r}\Big(h_{33,r} + \frac{\omega^2}{\omega^2 - \omega_e^2} h_{00,r} - \frac{K_e}{\omega^2 - \omega_e^2}\omega^2 N_{,r}\Big)\Big] dz. \tag{2.19}$$

$N(x^i)$ indicates the number density of the particles in the plasma around the black hole and $K_e = 4\pi e^2/m_e$ is a constant parameter. The signs $\pm$ of $\hat{\alpha}_b$ indicate deflection towards or away from the central object, respectively. At large distances, the black hole metric can be approximated as

$$ds^2 = \mathrm{d}s_0^2 + ...\mathrm{d}t^2 + ...\mathrm{d}r^2, \tag{2.20}$$

where $\mathrm{d}s_0^2 = -\mathrm{d}t^2 + \mathrm{d}r^2 + r^2(\mathrm{d}\theta^2 + \sin^2\theta \mathrm{d}\phi^2)$ and R_s is radius of schwarzschild. By utilizing the Eqs (2.2), (2.15), (2.18), we obtain the following values for the components of $h_{\alpha\beta}$ [57]

$$\begin{aligned} h_{00} =& \left(\frac{R_s}{r} - \frac{Q^2}{(1-l)^2 r^2} - \frac{l}{1-l}\right), \\ h_{ik} =& \left(\frac{R_s}{r} - \frac{Q^2}{(1-l)^2 r^2} - \frac{l}{1-l}\right) n_j n_k \;, \\ h_{33} =& \left(\frac{R_s}{r} - \frac{Q^2}{(1-l)^2 r^2} - \frac{l}{1-l}\right) \cos^2\kappa \;, \end{aligned} \tag{2.21}$$

where $\cos\kappa = \frac{z}{\sqrt{b^2+z^2}}$ and $r = \sqrt{b^2+z^2}$, b is the impact parameter signifying the closest approach of the photons to the black hole. By putting Eq. (2.21) into Eq. (2.19), we get following analytic formula for the deflection angle in vacuum case as

$$\alpha_b = \frac{2R_s}{b} - \frac{\pi l}{2(1-l)} - \frac{3\pi Q^2}{4(1-l)^2 b^2}\,. \tag{2.22}$$

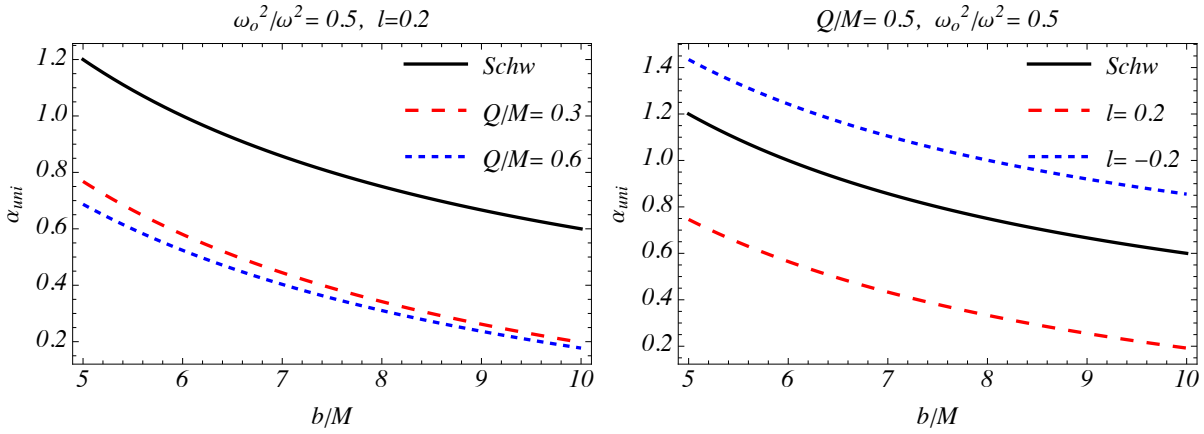

Figure 2.9: Plots of the deflection angle α_{uni} as a function of the impact parameter b for different Q/M charge of the black hole (left panel) and l parameter (right panel) in the case of constant plasma parameters ω_0^2/ω^2 .

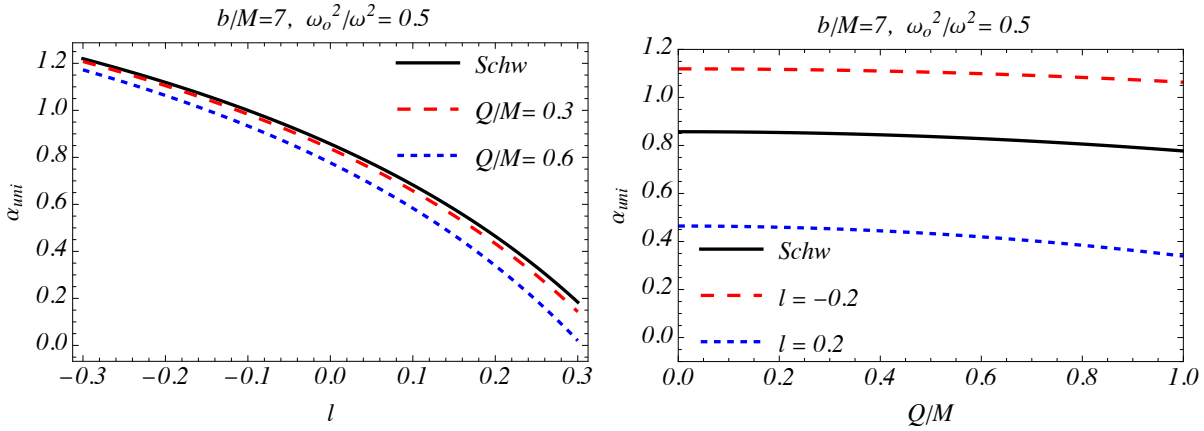

Figure 2.10: This graph describes the deflection angle α_{uni} as a function of the l (left panel) and Q/M parameters(right panel) depending on ω_0^2/ω^2 with a fixed parameter $b/M = 7$.

Uniform plasma

Initially, we investigate a homogenous plasma with a constant value of ω_0^2. In this scenario, the refractive index is not dependent on spatial coordinates, which enables us to ignore its impact on refraction. To put it more plainly, we exclude the final term from Eq. (2.19). The integration of Eq. (2.19) using Eq. (2.21) yields the following solution for the deflection angle in uniform plasma.

$$\alpha_{uni} = \frac{R_s}{b} - \frac{\pi Q^2}{4b^2(1-l)^2} - \frac{\pi l}{2(1-l)} + \frac{1}{1-\frac{\omega_0^2}{\omega 2}}\left(\frac{R_s}{b} - \frac{\pi Q^2}{2b^2(1-l)^2}\right) \tag{2.23}$$

Fig. 2.9 shows the impact parameter b for charge of the black hole Q (top panel) and l parameter (bottom panel) depending on plasma parameters ω_0^2/ω^2. Reducing the impact parameter b results in an increase in the deflection angle.

The bending angle achieves its maximum value due to the high distribution of plasma (shown Fig. 2.10 in the bottom panel). Additionally, it is observed that the bending angle decreases consistently as the l parameter increases (as shown in Fig. 2.10 top panel). For example, when considering Q and $l \to 0$, Schwarzschild gravity guarantees the highest degree of deviation, denoted as $\hat{\alpha}_{uni}$. If we compare our results with the Schwarzschild case, the negative value of the l parameter causes a larger deflection angle than in that case.

Singular isothermal spfere

The singular isothermal sphere (SIS) is the best suitable model for understanding the unique characteristics of photons that are gravitationally lensed. It was first used in [57] to investigate the properties of the galaxies and clusters through the lens. SIS is typically described as a spherical gas cloud with a singularity where the density tends to infinity at the cloud's center. A SIS's density distribution is provided by [57, 58]

$$\rho(r) = \frac{\sigma_\nu^2}{2\pi r^2} \tag{2.24}$$

where σ_ν^2 implies to a one-dimensional velocity. The following analytic dispersion can be used to characterize the plasma concentration [57, 58]

$$N(r) = \frac{\rho(r)}{\kappa m_p}, \tag{2.25}$$

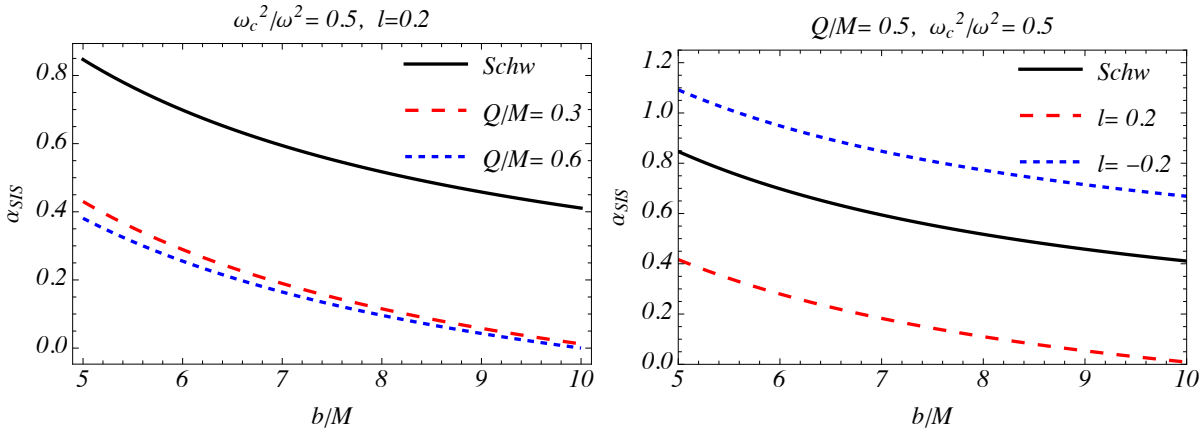

Figure 2.11: This graph describes a variation of $\hat{\alpha}_{sis}$ with respect to b in different the charge of black hole Q/M (top panel) and l (bottom panel) parameters.

Here, m_p represents the mass of the proton, and k is a dimensionless coefficient that is typically associated with the dark matter universe. Utilizing of Eqs. (2.24) and (2.25), the plasma frequency is expressed in this manner

$$\omega_e^2 = K_e N(r) = \frac{K_e \sigma_\nu^2}{2\pi\kappa m_p r^2}. \tag{2.26}$$

We consider the above-mentioned Eqs. (2.19),(2.21) and (2.26) and properties of the SIS, the bending of the light is written as

$$\alpha_{SIS} = \frac{2R_s}{b} - \frac{\pi l}{2(1-l)} - \frac{3\pi Q^2}{4b^2(1-l)^2} + \frac{R_s^2\omega_c^2}{2b^2\omega^2} + \frac{2R_s^2\omega_c^2}{\pi\omega^2}\left(\frac{R}{3b^3} - \frac{3\pi Q^2}{16b^4(1-l)^2}\right) \tag{2.27}$$

The analytic expression for the additional plasma constant ω_c^2 is given as follows [58]

$$\omega_c^2 = \frac{K_e \sigma_\nu^2}{2\pi\kappa m_p R_s^2}. \tag{2.28}$$

In order to analyze the impact of SIS on the path of the photon, we presented the relationship between the angle of deflection $\hat{\alpha}_{SIS}$ and the impact parameter b in Fig. 2.11. It is noticeable that both the uniform plasma and the SIS medium exhibit comparable characteristics in relation to the key parameter b. The amount ω_c^2/ω^2 represents the SIS distribution around a black hole. Through graphical

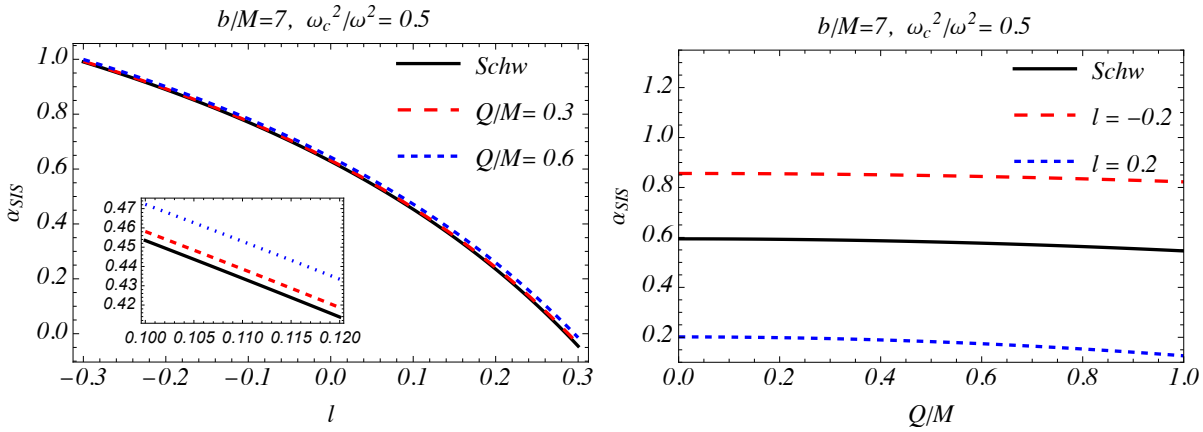

Figure 2.12: This graph illustrates a variation of $\hat{\alpha}_{sis}$ concerning the charge of black hole Q/M (left panel)and l(right panel) parameters in different ω_0^2/ω^2.

analysis in Fig. 2.12, we have observed the sensitivity of photons to the given parameter, as well as the black hole parameters Q and l. We observed a sharply drop in $\hat{\alpha}_{SIS}$ when parameter l increase. However, There is a gradual decrease in deflection angle with the increasing black hole charge. Consequently, the presence of SIS in the black hole's proximity affects massless particles to some extent.

Non singular isothermal sphere

Next, we will investigate the movement of photons when there is a non-singular isothermal sphere (NSIS) present. This choice is important because it offers a more realistic and practical context for our investigation. In contrast to the SIS, this plasma model confines the singularity within a finite core located at the center of the gas cloud. The density distribution within this core is described as follows [47, 57]:

$$\rho(r) = \frac{\sigma_\nu^2}{2\pi(r^2 + r_c^2)} = \frac{\rho_o}{1 + \frac{r^2}{r_c^2}}; \quad \rho_0 = \frac{\sigma_\nu^2}{2\pi r_c^2}, \tag{2.29}$$

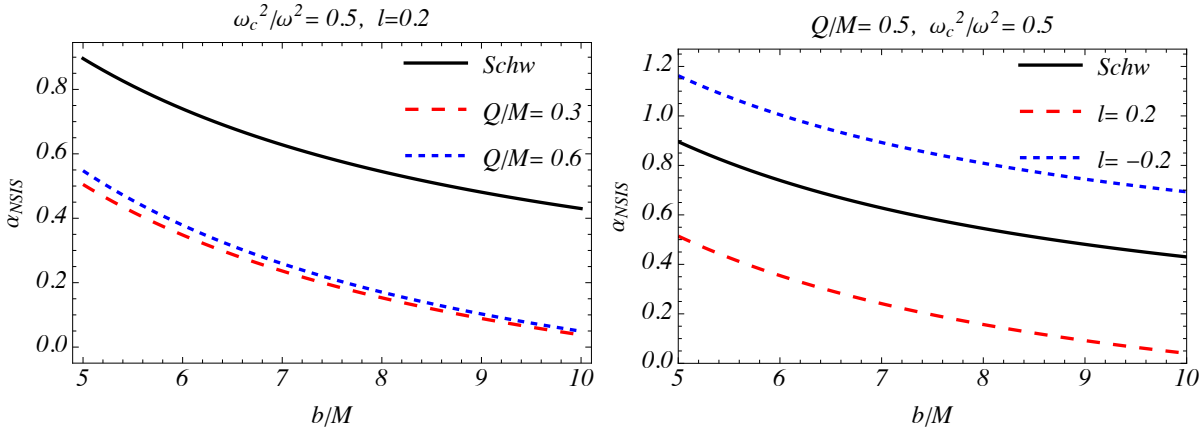

Figure 2.13: Plots of a variation of $\hat{\alpha}_{NSIS}$ depending on impact parameter b in various Q/M (top panel) and l (bottom panel) parameters depending on ω_0^2/ω^2.

here the radius of core is written by r_c. Plasma concentration in the NSIS model using Eq.(2.26) takes the form

$$N(r) = \frac{\sigma_\nu^2}{2\pi k m_p (r^2 + r_c^2)}. \tag{2.30}$$

From Eqs. (2.25), (2.28), and (2.30), we derive the frequency of plasma as follows

$$\omega_e^2 = \frac{K_e \sigma_\nu^2}{2\pi\kappa m_p (r^2 + r_c^2)}, \tag{2.31}$$

By doing analytical calculations utilizing equations (2.19), (2.21) and (2.31), we can get the following expressions for the deflection angle in the NSIS model.

$$\begin{aligned}\alpha_{NSIS} \;=\; & \frac{2R_s}{b} - \frac{\pi Q^2 R_s^2 \omega_c^2 (r_c^2 - 2b^2)}{2b^2(1-l)^2 {r_c}^4 \omega^2} - \frac{\pi b Q^2 R_s^2 \sqrt{\frac{1}{b^2+{r_c}^2}}\omega_c^2}{(1-l)^2 {r_c}^4 \omega^2} \\ & - \frac{b R_s^3 \omega_c^2 \tanh^{-1}\left(\frac{r_c}{\sqrt{b^2+{r_c}^2}}\right)}{{r_c}^3 \omega^2 \sqrt{b^2+{r_c}^2}} + \frac{\pi b R_s^2 \omega_c^2}{2\omega^2 \left(b^2+{r_c}^2\right)^{3/2}} \\ & + \frac{\pi Q^2}{4b^2(1-l)^2} + \frac{R_s^3 \omega_c^2}{b {r_c}^2 \omega^2} - \frac{\pi l}{2(1-l)}.\end{aligned} \tag{2.32}$$

In this case, the parameter $\frac{\omega_c^2}{\omega^2}$ is connected to the NSIS distribution. When comparing with the homogeneous plasma and SIS case it is difficult to notice the influence of $\frac{\omega_c^2}{\omega^2}$ from a specific point of view, as can be seen from Figs. Fig. 2.13

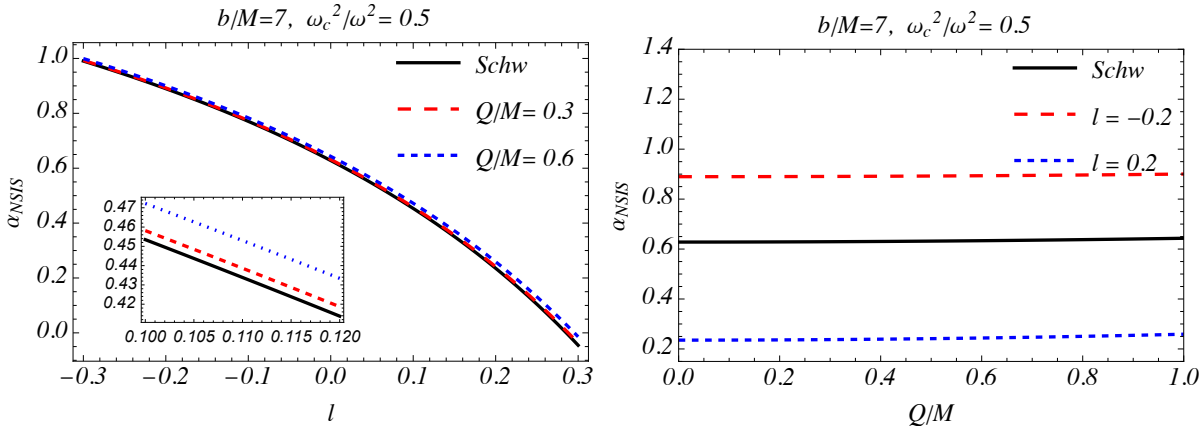

Figure 2.14: This figure illustrates a variation of $\hat{\alpha}_{NSIS}$ with respect to the charge of black hole Q/M (left panel) and l (right panel) parameter in different plasma frequency ω_0^2/ω^2.

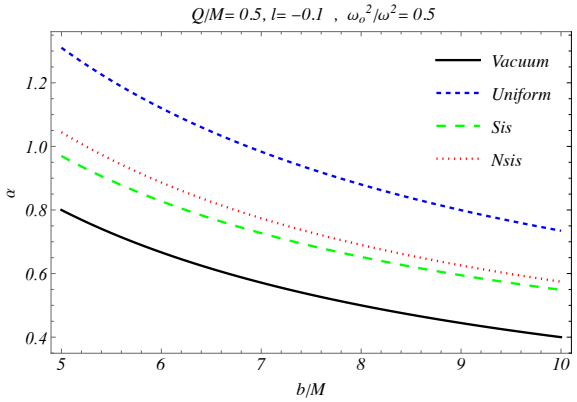

Figure 2.15: We compare bending of the light $\hat{\alpha}_b$ as a function of the impact parameter b. The fixed parameters are used as the following $\omega_0^2/\omega^2 = 0.5, \omega_c^2/\omega^2 = 0.5, r_c/M = 3$.

and 2.14, which show the behavior of the impact parameter b, the black hole's charge Q, and l parameter. However, with fixed l parameters and the black hole's charge, Fig. 2.15 presents a visual comparison of the $\hat{\alpha}_{uni}, \hat{\alpha}_{SIS}$, and $\hat{\alpha}_{NSIS}$ based on the impact parameter b. Compared to previous models, it is evident that the deflection angle is greatest in a homogeneous plasma medium. A mathematical equation representing the ultimate outcome is $\hat{\alpha}_{uni} > \hat{\alpha}_{nsis} > \hat{\alpha}_{sis} > \hat{\alpha}_{vac}$.

Lens equation and magnification

Next, we focus on the visible consequences of gravitational lensing, particularly the magnification of the brightness of the image source in the presence of plasma. In our previous sections, we explored the angle of deflection $\hat{\alpha}$, specifically focusing on a homogenous plasma. Fig. 2.16 is a schematic diagram of the gravitational lensing system, illustrating the source, the black hole acting as a lens, and the observer. To determine the image magnification of sources, it is best to use lens equation, which is connected with the source angular position β and image θ and distances from the source to the observer D_s and the lens D_{ls} and the angle of deflection [59–63]:

$$\theta D_s = \beta D_s + \hat{\alpha} D_{ds}. \tag{2.33}$$

We can approximate the $b \approx D_d\theta$ relation in the weak gravity. After that, we have the following expression.

$$\beta = \theta - \frac{D_{ds}}{D_s}\hat{\alpha}. \tag{2.34}$$

In the state of homogeneous plasma, after substituting Eq. (2.23) into Eq. (2.34) we can obtain a cubic equation for θ

$$a\theta^3 + b\theta^2 + c\theta + d = 0, \tag{2.35}$$

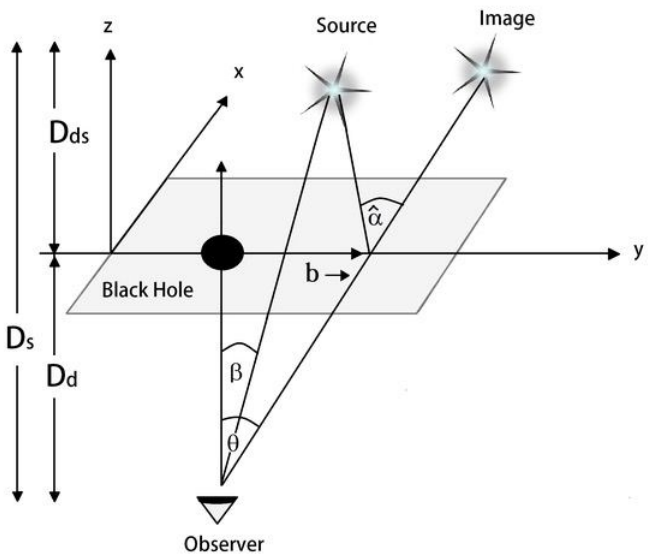

Figure 2.16: Schematic view of the gravitational lensing system [58]

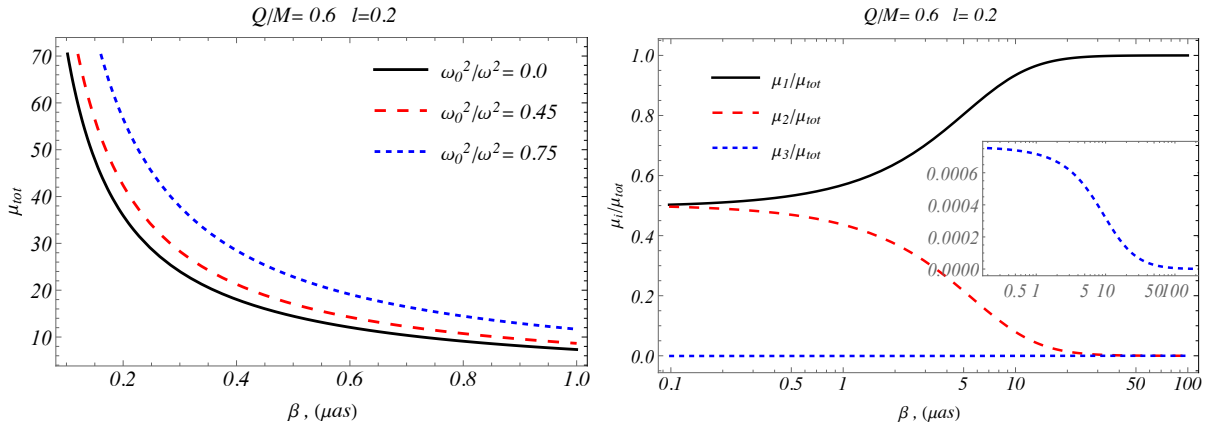

Figure 2.17: (left panel) Plots of the total magnification as a function of β. The fixed values were used as $Q/M = 0.6$, $l = 0.2$, and $M/D_d = 22.6 \cdot 10^{-12}$. (right panel) The magnification rate of the image source, as a function of the source position β, is given for $\omega_o^2/\omega^2 = 0.5$ and $M/D_d = 22.6 \cdot 10^{-12}$.

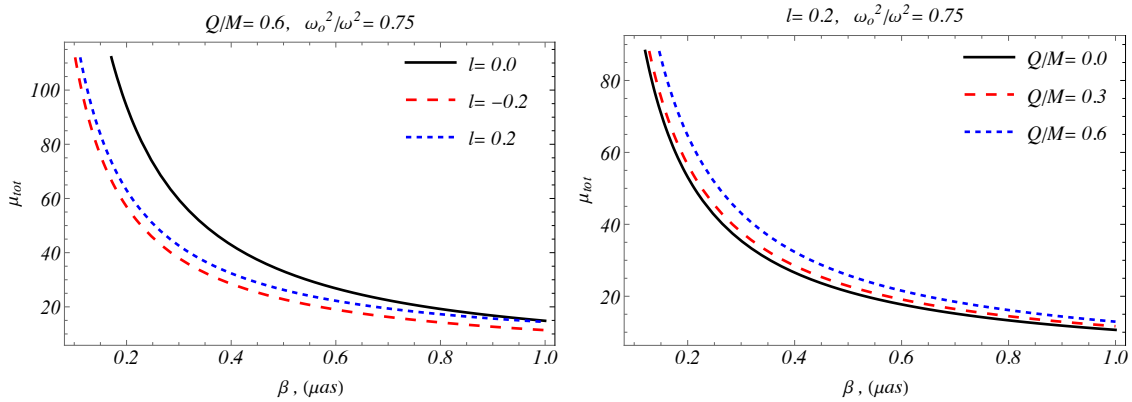

Figure 2.18: Graphs illustrate total magnification as a function of source position β for Q/M=0.6(left panel), $l = 0.2$(right panel) in fixed ω_o^2/ω^2=0.75 and $M/D_d = 22.6 \cdot 10^{-12}$

Table 2.1: This table gives information about magnification of images in both homogeneous plasma medium and vacuum cases. In this table $M/D_d = 2.26 \cdot 10^{-11}$ is used which corresponds to the supermassive black hole in the center of Milky Way, $\beta = 1\,\mu as$ and $D_s/D_{ds} = 2$(these parameters have taken from [60]).

$\mu_n/{\mu_n}^{\rm vac}$	ω_0^2/ω^2=0.1	ω_0^2/ω^2=0.5	ω_0^2/ω^2=0.9	$\mu_n^{\rm vac}$
$\mu_1/{\mu_1}^{\rm vac}$	1.024	1.19702	2.182	3.81604
$\mu_2/{\mu_2}^{\rm vac}$	1.03108	1.25513	2.53059	-2.94694
$\mu_3/{\mu_3}^{\rm vac}$	0.999983	0.980941	0.823	$-8.12076 \cdot 10^{-14}$

where

$$a = 1,\ b = \frac{\pi l}{4(1-l)} - \beta,\ c = -\frac{M}{D_d}\left(\frac{1}{1-\frac{\omega_0^2}{\omega 2}} + 1\right),$$
$$d = \frac{\pi Q^2}{8(1-l)^2}\frac{M^2}{D_d^2}\left(1 + \frac{2}{1-\frac{\omega_0^2}{\omega 2}}\right). \tag{2.36}$$

After creating a new variable $\theta = y - \frac{b}{3a}$, we can convert Eq. (2.35) to this equation [64]

$$y^3 + py + q = 0, \tag{2.37}$$

where

$$p = \frac{c}{a} - \frac{b^2}{3a^2};\ q = \frac{2b^3}{27a^3} - \frac{bc}{3a} + \frac{d}{a}. \tag{2.38}$$

It is better to use the Einstein ring θ_E, which is given below instead of $\frac{M}{D_d}$

$$\theta_E = \sqrt{\frac{2R_s D_{ds}}{D_s D_d}}\ . \tag{2.39}$$

Then we obtain the solution of Eq. (2.37) which is written as [65]

$$x = 2s^{1/3}\cos\frac{\phi + 2k\pi}{3}, \tag{2.40}$$

where

$$s = \sqrt{-\frac{p^3}{27}}\ , \quad \phi = \arccos\left(-\frac{q}{2s}\right). \tag{2.41}$$

The ratio of the observer's solid angles to the source, summed for each image, yields the overall magnification of the pictures. The overall magnification, μ_Σ, is roughly given as follows in the weak-field approximation [47]

$$\mu_\Sigma = \frac{I_{\rm tot}}{I_*} = \sum_k \left|\left(\frac{\theta_k}{\beta}\right)\left(\frac{{\rm d}\theta_k}{{\rm d}\beta}\right)\right|, \quad k = 1, 2, ..., n \tag{2.42}$$

where $\theta_k = y - \frac{b}{3a}$. There are three components of the magnification of the images, ordinary two images and relativistic images that appeared due to the presence of the Q/M and l parameters. Using mathematical calculations, one can obtain a numerical equation that represents the total magnification of an image. In Fig. 2.17, the left panel shows the overall magnification of the image based on the angular position β of the source. It exhibits different values of the black hole charge Q and l quantities. An increase in the value of the position β results in a reduction in total magnification. Furthermore, it is evident that the expansion of the magnification is influenced by the presence of plasma medium. (For the panel on the right). These graphs demonstrate how the magnification rates in the uniform and vacuum cases differ, with the primary image having a higher rate than the secondary and relativistic images. In Fig. 2.18, a graph is shown that illustrates the relationship between total magnification and source position

β for various values of the parameter l (left panel) and the parameter Q (right panel). It is evident that an increase in the parameter Q results in a higher total magnification. In contrast, the growth in β leads to a decrease in total magnification.

In Table 2.1, for Sgr A* we compare the magnification of the images surrounded by the uniform plasma and vacuum cases. One can notice that the magnification of the third image decreases in the presence of plasma. In contrast, decreasing plasma frequencies cause increasing magnification of primary and secondary images. Additionally, we found the position of the image, angle of deflection, and magnification of the images for various galaxies. Table 2.2. provides the values of these quantities for different galaxies with fixed Q and l parameters.

Table 2.2: The estimated values of angular positions and magnifications of primary, secondary, and relativistic images at the centers of many galaxies. The symbols θ and μ represent angular positions and magnifications, respectively. The initial column provides the names of galaxies. The subscripts sec, primary, and rel indicate the secondary, primary, and relativistic images, respectively. The angular quantities represented by μas are all encompassing. The distance values, denoted as M/D_d, are obtained from the source cited as [60]. The angular position of the source. Relativistic images that are located on the same side as the main image. All calculation is done with $\beta = 1(\mu as)$, $Q/M = 0.6, l = 0.2$ and ω_o^2/ω^2=0.5.

	Secondary∗		Primary∗		Relativistic∗	
MDO in galaxy	θ_{sec}	μ_{sec}	θ_{pri}	μ_{pri}	θ_{rel}	μ_{rel}
Milky Way	-7.7766	3.69878	8.71115	4.56788	0.0654582	$6.68339 \cdot 10^{-14}$
NGC4486(M87)	-4.71765	2.17602	5.6522	3.04512	0.0654531	$2.63347 \cdot 10^{-14}$
NGC4342	-1.28404	0.494715	2.21859	1.36382	0.0654502	$2.87024 \cdot 10^{-15}$
NGC5845	-0.75352	0.252749	1.68807	1.12185	0.06545	$1.31159 \cdot 10^{-15}$
NGC3031(M81)	-1.16422	0.438739	2.09877	1.30784	0.0654502	$2.47059 \cdot 10^{-15}$
CygnusA	-0.909065	0.321831	1.84361	1.19093	0.0654501	$1.71124 \cdot 10^{-15}$
NGC4291	-0.895911	0.315912	1.83046	1.18501	0.0654501	$1.67854 \cdot 10^{-15}$
NGC7052	-0.51683	0.1529	1.45138	1.022	0.0654499	$8.1747 \cdot 10^{-16}$

2.5 Conclusion

This research investigates the behavior of an RN-like black hole in KR gravity. The study focuses on analyzing null geodesics, shadows, and weak gravitational lensing in both homogeneous and inhomogeneous plasma settings.

When studying the weak gravitational field limit, it becomes clear that the presence of black hole charge Q causes a reduction in the bending of light. Compared to the Schwarzschild case, the negative value of the parameter l results in a higher deflection angle of light around the black hole, whereas the positive value of l leads to a lower deflection angle.

Also, we have studied the influence of plasma in the radius of the photon sphere, black hole's shadow, angle of deflection of light rays, and magnification rate. Increasing the plasma parameter causes the radius of the photon and the shadow to decrease in the case of an inhomogeneous plasma medium ($q = 3$) when the plasma parameter is growth. When the plasma parameter of a non-uniform plasma medium ($q = 1$) increases, the radius of the photon sphere correspondingly increases, but the shadow of the black hole decreases. Moreover, the presence of plasma leads to an increase in both the angle of deflection and the magnification of the pictures.

Besides, we have constraints on the shadow of Sgr A* black hole. Our results exactly coincide with observational data that were token from the EHT. We also determined that while the Lorentz violation parameter l was increasing, the radius of the BH's shadow started reducing and it is clearly shown in Fig. 2.8.

Chapter III

Astrophysical properties of black holes in asymptotically safe gravity

In this chapter we investigate the motion of neutral test particles around a non-rotating regular black hole within the framework of asymptotically safe gravity, analyzing the impact of the black hole's parameters on particle motion. This black hole solution is characterized by an additional parameter, η, which differentiates it from the standard Schwarzschild black hole solution. We obtain analytical formulations for the energy and angular momentum of equatorial circular orbits as functions of the black hole parameter. The stability of these circular orbits is examined by the effective potential. Additionally, we present a graphical study of the innermost stable equatorial circular orbits as functions of the black hole parameter and investigate the effective force exerted on circular orbits. We also derive the frequencies of radial and latitudinal harmonic oscillations as functions of the model parameters and discuss the key features of quasi-periodic oscillations of test particles near stable circular orbits in the black hole's equatorial plane. The phenomenon of periastron precession is also considered. Additionally, we explore particle collisions near the black hole and demonstrate that such collisions can produce high energy near the event horizon. Our findings indicate that the

black hole parameter significantly influences the motion of test particles around a regular black hole in the context of asymptotically safe gravity. We examine the shadow of black hole and using observational data from the Event Horizon Telescope (EHT) collaboration for Sgr A* and M87*, we have determined the range of η parameter that corresponds to the observations.

3.1 Introduction

Black holes (BHs) are unusual cosmic entities with enormous gravitational forces. Typically, nothing escapes a BH's event horizon due to its enormous gravitational attraction, which absorbs everything within its domain. These thermodynamic objects not only exhibit extraordinary classical characteristics but also improve our understanding of quantum gravitational phenomena. Curvature singularities are found behind the event horizons of the most well-investigated BH configurations. Regular black holes are those that prevent singularities from approaching their horizons. These BHs are particularly beneficial in high-energy collisions and need finite amounts of energy to create. Bardeen [66] proposed a regular BH model by analyzing the collapse of electrically charged matter with an Ads core within the BH, which replaced the singularity. Subsequently, several regular BH models have been developed using alternative matter sources [67–71] or in different gravity theories [72–76]. Similar efforts have been attempted to include quantum corrections, at least from a phenomenological point of view [77–79], or by singularity regularization [80].

In addition, a significant focus has been placed on the idea of asymptotic safety [81,82]. Recently, Bonanno et al. [82] introduced a novel model of a regular BH inspired by the theories of Markov and Mukhanov, employing the notion of gravity's anti screening properties in ultra-Planckian energy regimes. They pro-

vided a detailed metric characterizing the outside of the collapsing dust sphere within the context of asymptotically safe gravity. It is presumed that quantum adjustments, which obscure the singularity within a BH, operate on Planck scales and are unlikely to generate discernible astrophysical impacts since, far from the event horizon, the BH's geometry resembles Schwarzschild. Consequently, a natural inquiry emerges as to how these quantum modifications can be potentially detectable. The detection of black hole shadows [83] and recent detections of gravitational wave emissions from stellar-mass black hole mergers [84] provide a chance to examine intricate gravitational phenomena specific to compact relativistic entities, thereby generating new avenues for fundamental physics inquiry [85]. In this context, numerous investigations have investigated the quasi normal modes [86] and black hole shadows [87] of various ordinary black holes.

In astrophysics, the motion of particles, whether test particles or charged/neutral particles around a BH, is crucial. In addition to helping explain energetic processes that take place close to the event horizon of a BH, this study offers important insights into the large-scale structure of spacetime [88–96]. These phenomena encompass the emission of jets (arising from particle ejection in a magnetic field), accretion disks (particles orbiting the black hole), and the acceleration of cosmic rays and gamma rays. The acceleration of cosmic and gamma rays is a vital area of investigation in astronomy, with active galactic nuclei serving as primary candidates for the acceleration of ultra-high-energy cosmic rays [97, 98]. Examining particle dynamics in curved spacetime enhances our understanding of spacetime characteristics. There is a great deal of literature on particle motion around many types of BHs, including brane-world BHs [99, 100], quantum corrected BHs [101, 102], anti-de Sitter BHs [103, 104], Schwarzschild MOG BHs [105] and Kerr MOG BHs [106].

We investigate a normal black hole's shadow in asymptotically safe gravity. Under little perturbations, photons on unstable orbits either fall into the black hole or escape to infinity, creating the black hole shadow. The shadow is formed by these photons' creation of light rings that are projected onto an observer's screen. Strong gravitational lensing causes the light beams to travel close to the event horizon, making the shadow an important indicator of strong field gravity. Prominent studies by Synge [107] and Luminet [108] defined the Schwarzschild black hole shadow and determined the angular radius of photons. This was extended to spinning Kerr black holes to demonstrate how rotation distorts the shadow in Bardeen's study [109]. Research indicates that the shadows of various types of black hole can be used to evaluate gravitational theories and elucidate black hole properties.

In this chapter, we discuss the orbital motion of test particles moving around a regular BH within asymptotically safe gravity. The stability of circular orbits, innermost stable circular orbits (ISCOs), and the effective force acting on test particles have been discussed. We discuss the shadows of the examined BH. Furthermore, collisions of particles and the center-of-mass energy have been investigated. In Section 3.2, we describe the essential characteristics of the BH spacetime under investigation. Section 3.3 explores the trajectory of test particles in the vicinity of a normal black hole within the framework of asymptotically safe gravity. The stability of equatorial circular orbits has been analyzed using effective potentials, innermost stable circular orbits (ISCOs), and the effective force acting on particles. The epicyclic oscillations and perturbed circular orbits are considered in Section 3.4 and constraints on the mass of regular black holes are obtained in the framework of asymptotically safe gravity in Section 3.6. We examine shadow behaviors and offer predictions for η using the EHT data in Section 3.7. Section

3.8 contains the concluding findings.

3.2 Regular black holes in the framework of the asymptotically safe gravity

We begin with a brief review of a non-rotating regular BH in the background of asymptotically safe gravity. Recently, Bonnano et al. [82] expanded on the concepts introduced by Markov and Mukhanov [110], examining the formation of regular BH during gravitational collapse. They address this through the following action

$$I = \frac{1}{16 G_N \pi} \int (R + 2\mathcal{Y}(\epsilon)\mathrm{L})\sqrt{-g}\, d^4x, \tag{3.1}$$

where L denotes the matter Lagrangian, and $\mathcal{Y}(\epsilon)$ ($\mathcal{Y}(0) = 8G_N\pi$) some coupling Lagrangian. The total variation of the action (3.1) gives the following differential equations

$$R_{\alpha\beta} = \frac{R\, g_{\alpha\beta}}{2} = 8\pi T_{\alpha\beta} G(\epsilon) - g_{\alpha\beta}\, \Lambda(\epsilon), \tag{3.2}$$

where

$$T_{\alpha\beta} = (p(\epsilon) + \epsilon) u_\alpha u_\beta + p g_{\alpha\beta}, \tag{3.3}$$

denotes the energy-momentum tensor of the ideal fluid, while $\Lambda(\epsilon)$ and $G(\epsilon)$ represents the cosmological constant and effective gravitational constant, given by

$$\Lambda(\epsilon) = \frac{\partial \mathcal{Y}}{\partial \epsilon}\epsilon^2, \tag{3.4}$$

$$8\pi G(\epsilon) = \frac{\partial(\mathcal{Y}\epsilon)}{\partial \epsilon}. \tag{3.5}$$

A renormalization group trajectory closer to the ultraviolet fixed point of the asymptotic safety program [82] determines the behavior of $G(\epsilon)$ with regard to the function of the energy scale and was considered as:

$$G(\epsilon) = \frac{G_N}{1 + \eta\epsilon}, \tag{3.6}$$

where G_N is the gravitational constant, while the parameter η is the scale parameter. Some observations from [111, 112] can be used to constrain the unknown value of the scale parameter η. The following metric for static outside space-time was generated by the authors [82] as a result of the gravitational collapse of dust $(p = 0)$ as:

$$ds^2 = -f(r)dt^2 + f^{-1}(r)dr^2 + r^2(d\theta^2 + sin^2\theta\ d\phi^2), \tag{3.7}$$

where the unknown function $f(r)$ reads

$$f(r) = 1 - \frac{r^2}{3\eta}\ln\left(\frac{6M\eta}{r^3} + 1\right), \tag{3.8}$$

where M is the Gravitational mass. For vanishing $\eta = 0$, the metric (3.7) leads to the Schwarzshild metric. The position of the horizon is calculated by solving the equation $f(r) = 0$, which can give interesting results. For any specified value of M, critical values exist given by

$$\eta_{cr} = \frac{2}{3}(3 + 2y)y^2M^2, \tag{3.9}$$

and

$$r_h^{ext} = -2My, \quad y = W_0(x) = W_0(-\frac{3}{2e^{\frac{3}{2}}}), \tag{3.10}$$

where $W_0(x)$ defines the Lambert function and the numerical values are provided as:

$$\eta_{cr} = 0.4565M^2, \quad r_{\text{hoz}}^{ext} = 1.2516M. \tag{3.11}$$

There are the following situations

- For $\eta \in (0, \eta_{cr})$, there exist two roots of $f(r)$ that correspond to the inner horizon $(r_{\text{hor}} \in (0, r_{\text{hoz}}^{ext}))$ and the outer horizon $(r_{\text{hor}} \in (r_{\text{hoz}}^{ext}, 2M))$. However, for small values of η, the outer horizon can be approximated as

$$r_{\text{hoz}} = 2M - \frac{3\eta}{4M} - \frac{15\eta^2}{32M^3} + O(\eta^3). \tag{3.12}$$

- For $\eta = \eta_{cr}$, the outer and inner event horizons merge into a single horizon at $r_{\rm hoz} = r_{\rm ext}$, resulting in an extremal BH solution.

- For $\eta > \eta_{\rm cr}$, a horizonless configuration arises. For η approaches 0, the Schwarzschild solution can be obtained.

3.3 Motion of particles around regular black holes within asymptotically safe gravity

The Newtonian describes the motion of a neutral particle as:

$$H = \frac{1}{2} g^{\alpha\beta} P_\alpha P_\beta + \frac{1}{2} m^2, \tag{3.13}$$

where m represents the mass of the particle, $P^\alpha = mU^\alpha$ signifies the four momentum, $U^\alpha = dx^\alpha/d\tau$ indicates the four speed, and τ denotes the proper time of the test particle. The Hamiltonian equations of motion are expressed as:

$$\frac{dx^\alpha}{d\zeta} \equiv mU^\alpha = \frac{\partial H}{\partial P_\alpha}, \quad \frac{dP_\alpha}{d\zeta} = -\frac{\partial H}{\partial x^\alpha}, \tag{3.14}$$

where $\zeta = \tau/m$ represents the affine parameter. Owing to the symmetries of the black hole geometry, two constants of motion are present: a specific energy E and specific angular momentum L, which both are defined as follows

$$\frac{P_t}{m} = -\left(1 - \frac{r^2}{3\eta} \ln\left(\frac{6M\eta}{r^3} + 1\right)\right) \frac{dt}{d\tau} = -\mathcal{E}, \tag{3.15}$$

$$\frac{P_\phi}{m} = r^2 \sin^2\theta \, \frac{d\phi}{d\tau} = \mathcal{L}, \tag{3.16}$$

where $\mathcal{E} = E/m$ and $\mathcal{L} = L/m$ denote a particular energy and a specific angular momentum, respectively. The temporal U^t, azimuthal U^ϕ and radial U^r

components of the four-velocity U^{α} adhere to the following equations as:

$$\dot{t} = \frac{\mathcal{E}}{1-\frac{r^2}{3}\eta\ln\left(\frac{6M\eta}{r^3}+1\right)}, \tag{3.17}$$

$$\dot{\phi} = \frac{\mathcal{L}}{r^2\sin^2\theta}, \tag{3.18}$$

$$\dot{r}^2 + \left(\delta+\frac{L^2}{r^2\sin^2\theta}\right)f(r) = \mathcal{E}^2, \tag{3.19}$$

where $\delta = 1$ for time-like particles and $\delta = 0$ for null particles. The dot represents the derivative for the appropriate time τ. Our effort will concentrate exclusively on time-like particles. The Hamiltonian (3.13) for a conventional black hole (3.7) under the framework of asymptotically safe gravity is expressed as

$$\begin{aligned} H = {} & \frac{1}{2}\left(1-\frac{r^2}{3\eta}\ln\left(\frac{6M\eta}{r^3}+1\right)\right)P_r^2+\frac{1}{2r^2}P_\theta^2 \\ & +\frac{1}{2}\frac{m^2}{\left(1-\frac{r^2}{3\eta}\ln\left(\frac{6M\eta}{r^3}+1\right)\right)}\left[V_{\text{eff}}(r,\theta)-\mathcal{E}^2\right], \end{aligned} \tag{3.20}$$

where the effective potential $V_{eff}(r,\theta)$ can be written as

$$V_{eff}(r,\theta) = \left(1+\frac{\mathcal{L}^2\csc^2\theta}{r^2}\right)\left(1-\frac{r^2}{3\eta}\ln\left(\frac{6M\eta}{r^3}+1\right)\right). \tag{3.21}$$

For $\eta = 0$, the effective potential (3.21) leads to the Schwarzschild case.

Equatorial circular orbits

The effective potential $V_{eff}(r,\theta)$ is crucial for understanding the dynamics of the test particles. It provides a means to describe the motion of particles independently of explicit equations of motion. The stable and unstable circular orbits correspond to the minimum and maximum values of V_{eff}, respectively. The behavior of the effective potential for the equatorial orbits is shown in Fig. 3.1. In the first row and first column, the behavior of effective potential is shown for different values of the BH parameter η, while the behavior of effective potential

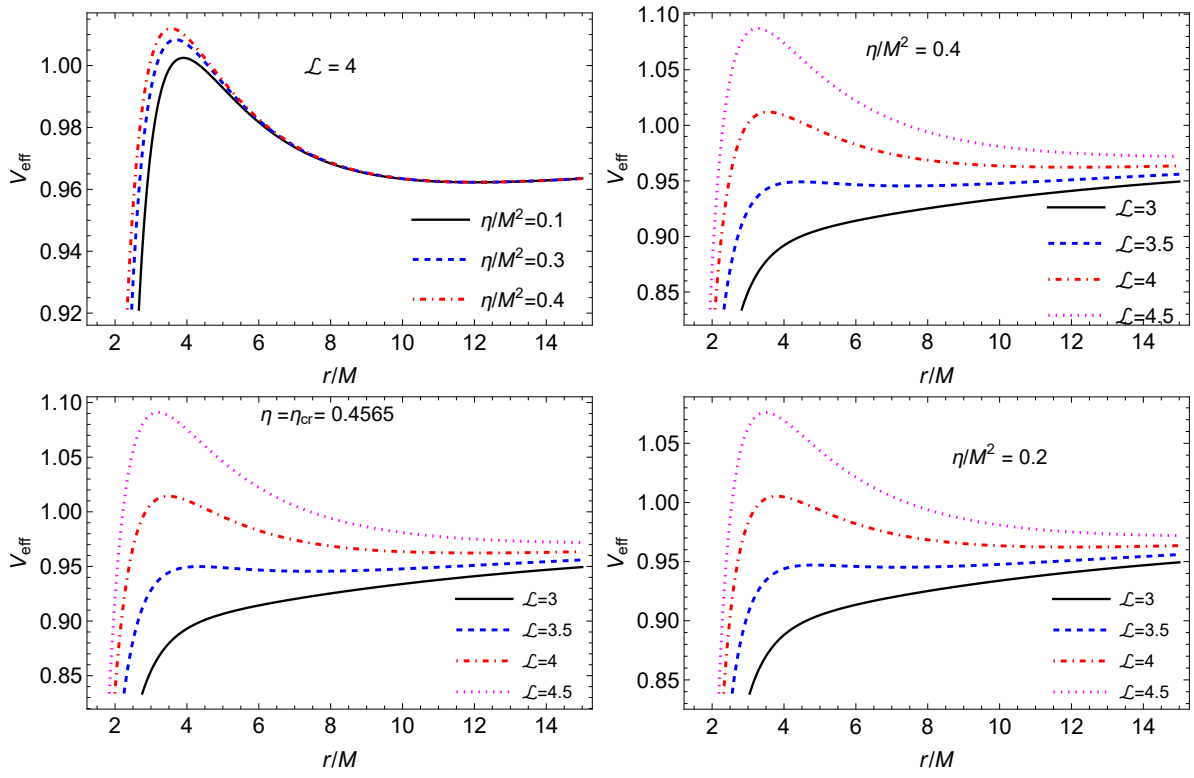

Figure 3.1: Behaviour of the effective potential for the test particles in the background of regular BH in asymptotically safe gravity.

for different values of angular momentum $\mathcal{L}$ is shown for $\eta < \eta_{cr}$ and $\eta = \eta_{cr}$. When $\eta < \eta_{cr}$, the effective potential does not increase much as we increase the values of angular momentum. It is interesting to note that both the BH parameter η and the particle's angular momentum $\mathcal{L}$ behave similarly on effective potential. The effective potential increases with increasing either the BH parameter η or the angular momentum of the particle $\mathcal{L}$. When the particles move close to the event horizon of the BH, the circular orbits are stable, and stability decreases as the particles move away from the BH. The circular orbits in an equatorial plane $\theta = \pi/2$ can be found by the simultaneous conditions

$$V_{\text{eff}}(r) = \mathcal{E}^2, \quad \frac{dV_{\text{eff}}(r)}{dr} = 0. \tag{3.22}$$

To resolve Eq. (3.22), we derive the circular orbits within the context of a non-rotating regular black hole with asymptotically safe gravity (3.7), expressed as

$$\mathcal{L} = \frac{r^2\sqrt{\frac{9M}{6\eta M+r^3} - \frac{\ln\left(\frac{6\eta M}{r^3}+1\right)}{\eta}}}{\sqrt{3 - \frac{9Mr^2}{6\eta M+r^3}}}, \tag{3.23}$$

and

$$\mathcal{E} = \frac{3\eta - r^2\ln\left(\frac{6\eta M}{r^3}+1\right)}{3\eta\sqrt{1 - \frac{3Mr^2}{6\eta M+r^3}}}. \tag{3.24}$$

For $\eta = 0$, the Eqs. (3.23) and (3.24) reduces to the case of Schwarzschild BH. Figure 3.2 describes the behavior of the energy as a function of r for varying values of the BH parameter η. It is shown that when the value of the BH parameter η is small, the particles have a large energy; however, the energy behavior decreases for large values of η. The behavior of the angular momentum increases monotonically as the radial distance r increases. Figure 3.2 describes the behavior of the energy as a function of r for varying values of the BH parameter η. It is shown that when the value of the BH parameter η is small, the particles have a

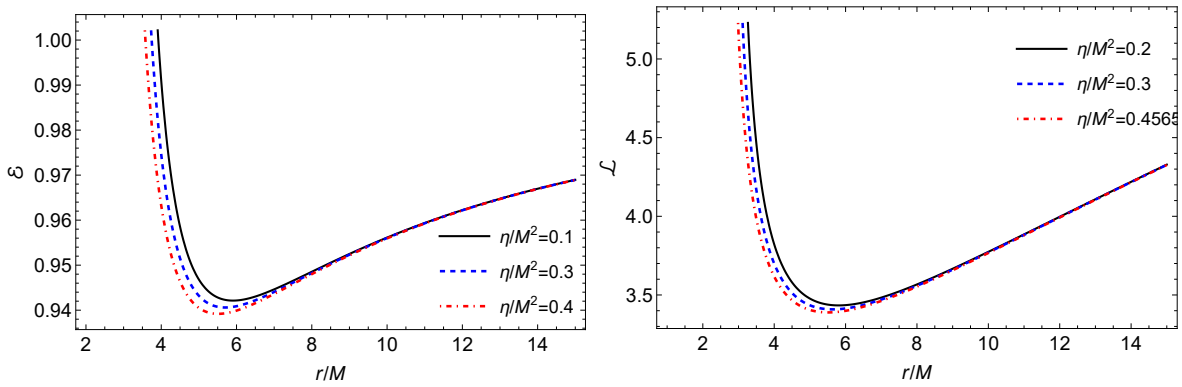

Figure 3.2: Behavior of energy (left) and angular momentum (right) of the circular orbits as a function of r in the background of regular BH in asymptotically safe gravity.

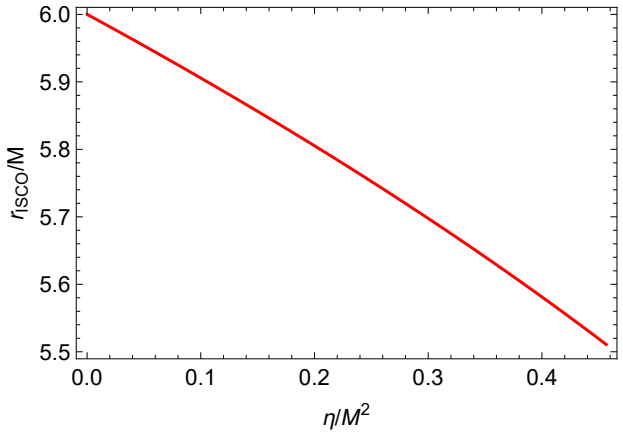

Figure 3.3: Behaviour of the ISCOs of particles, as a function of BH parameter η/M^2 in the background of regular BH in asymptotically safe gravity.

large angular momentum, while the particles have a small angular momentum for increasing values of the BH parameter η. However, the behavior of the angular momentum increases monotonically as the radial distance r increases.

Regular black holes in asymptotically safe gravity and innermost stable circular orbits

The extremum of the effective potential signifies the positions of stable and unstable circular orbits, respectively. In Newtonian theory, the effective potential exhibits a minimum radius that corresponds to the Innermost Stable Circular Or-

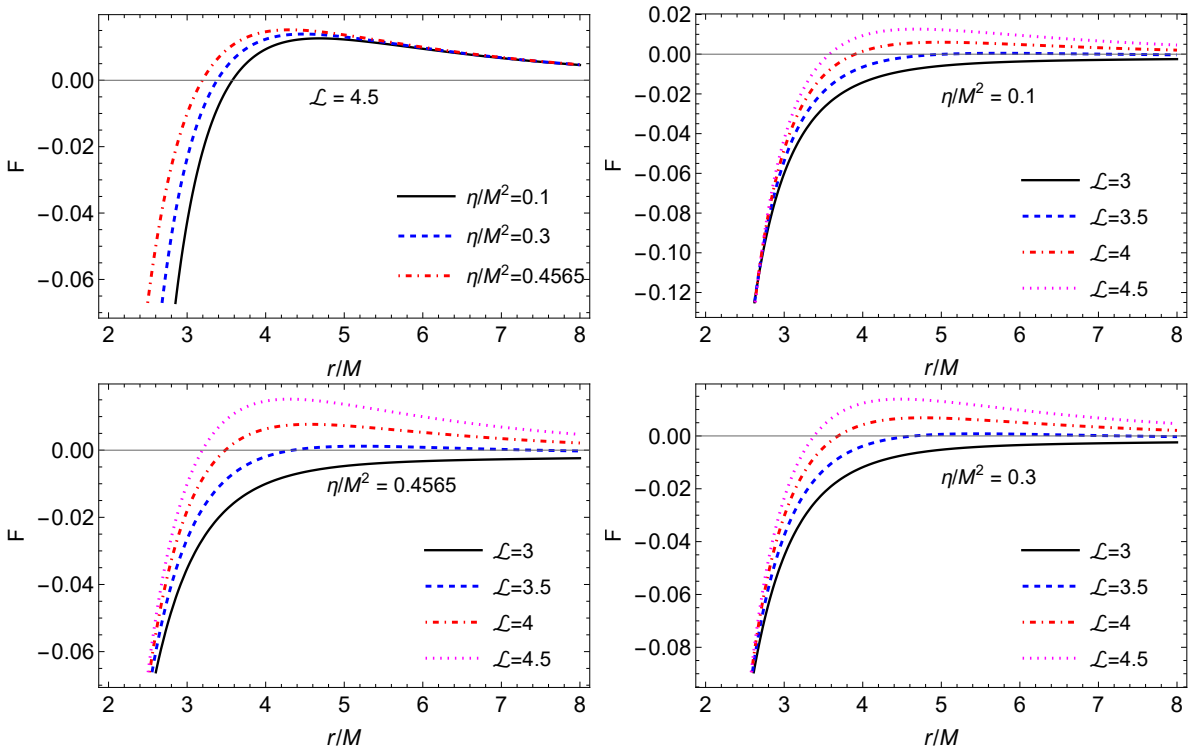

Figure 3.4: Behaviour of effective force acting on particles in the background of regular BH in asymptotically safe gravity.

bit (ISCO) for any specified angular momentum. Nevertheless, as elements such as the particle's rotational momentum and other attributes affect the effective potential, its structure becomes more intricate, resulting in alterations to the positions of these circular orbits. Thus, in General Relativity, the effective potential for particles nearing a Schwarzschild black hole can display two extreme states for a specified angular momentum. An accurate calculation of the angular momentum is essential for discussing the position of the ISCO in the current analysis. The locations of ISCOs can be determined according to the specified requirements by taking following relations:

$$V_{\text{eff}}(r) = \mathcal{E}^2, \quad \frac{dV_{\text{eff}}(r)}{dr} = 0, \quad \frac{d^2V_{\text{eff}}(r)}{dr^2} = 0. \tag{3.25}$$

The radii of ISCOs for the present non-rotating regular black hole in the context of asymptotically safe gravity can be determined using the last expression of Eq.

(3.25). The behavior of equatorial ISCOs surrounding a non-rotating regular black hole within the context of asymptotically safe gravity is illustrated in Fig. 3.3. The behavior is depicted as a function of the BH parameter η. The radii of the ISCOs decrease as the BH parameter η increases. The ISCOs surrounding non-rotating regular black holes in the context of asymptotically safe gravity are less than those associated with the Schwarzschild black hole.

Effective force

The net force exerted on a particle indicates its velocity, which indicates whether it is being dragged into the black hole or going away from it. We examine the particle's motion in the context of a non-rotating regular BH within asymptotically safe gravity, where both attractive and repulsive gravitational forces can occur. Using Eq. (3.22), we determine the effective force acting on the particles, which is given by

$$F = -\frac{1}{2}\frac{dV_{eff}}{dr}, \tag{3.26}$$

for the current BH solution, it is calculated as:

$$F = \frac{3\eta\mathcal{L}^2\left(6\eta+(r-3)r^2\right)-9\eta r^4+F_1}{2\sqrt{3}\eta r^2\left(6\eta+r^3\right)F_2}, \tag{3.27}$$

where

$$F_1 = r^4\left(6\eta+r^3\right)\ln\left(\frac{6\eta}{r^3}+1\right),$$
$$F_2 = \sqrt{\frac{\left(\mathcal{L}^2+r^2\right)\left(3\eta-r^2\ln\left(\frac{6\eta}{r^3}+1\right)\right)}{\eta}}.$$

The behavior of the effective force around the non-rotating regular BH in the background of asymptotically safe gravity is shown in Figure 3.4, as a function of r, for the parameter of varying values of BH η and the angular momentum. It is

noted that the effective force acting on the particles has the same behavior for both the parameters η and the angular momentum. The effective force is small when the parameter η or the angular momentum $\mathcal{L}$ has small values, however, the effective force increases when the parameter η or angular momentum $\mathcal{L}$ increases. When we fix the angular momentum and vary the BH parameter η, the effective force radial profiles coincide as the radial distance r increases. However, for varying values of angular momentum, different radial profiles of effective force can be observed as the radial distance r increases.

3.4 Epicyclic oscillations and perturbed circular orbits

To examine the oscillatory motion of neutral particles, we perturb the equations of motion near ISCOs. A test particle displaced marginally from the equilibrium point of a stable circular orbit in the equatorial plane will experience epicyclic motion, defined by linear harmonic oscillations.

Frequencies measured by local observer

The frequencies of harmonic oscillatory motion measured by the local observer are given by

$$\omega_r^2 = -\frac{1}{2}\frac{\partial^2 V_{\text{eff}}(r,\theta)}{\partial r^2}, \tag{3.28}$$

$$\omega_\theta^2 = \frac{1}{2}\frac{g_{rr}(r,\theta)}{r^2}\frac{\partial^2 V_{\text{eff}}(r,\theta)}{\partial \theta^2}, \tag{3.29}$$

$$\omega_\phi = \frac{d\phi}{d\tau}. \tag{3.30}$$

The radial (ω_r), latitudinal (ω_θ), and orbital/axial (ω_ϕ) frequencies of the neutral test particle around non-rotating regular BHs within asymptotically safe

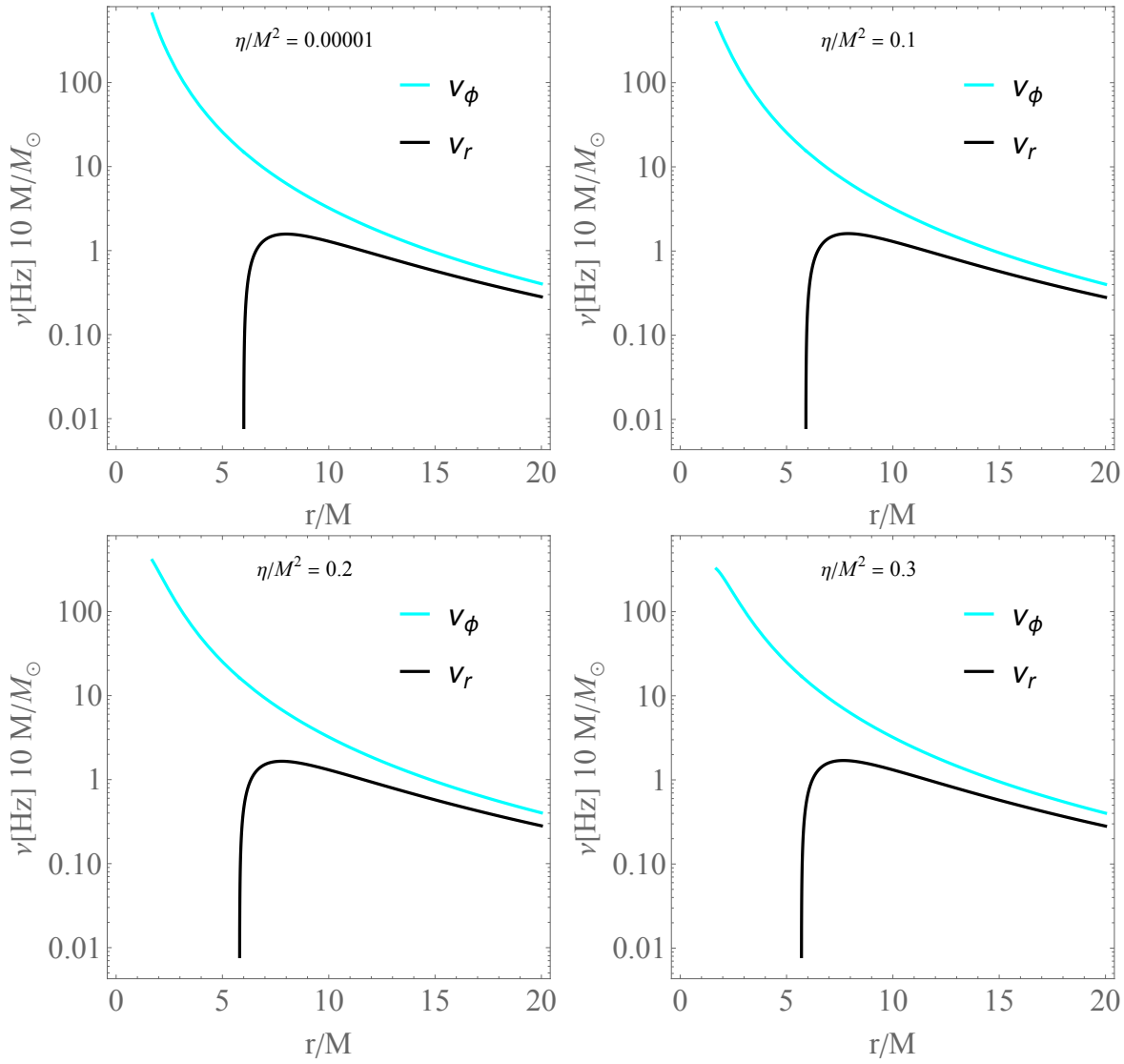

Figure 3.5: Frequencies of particles moving around regular BHs within asymptotically safe gravity, for different values of BH parameters η.

gravity takes the form

$$\omega_r^2 = \frac{1}{\mathcal{Z}_1}\left(\mathcal{Z}_2\mathcal{Z}_3\left(L^2+r^2\right)+\mathcal{Z}_4\right), \tag{3.31}$$

$$\omega_\theta^2=\omega_\phi^2 = \frac{9\eta M-\left(6\eta M+r^3\right)\ln\left(\frac{6\eta M}{r^3}+1\right)}{3\eta\left(6\eta M-3Mr^2+r^3\right)}, \tag{3.32}$$

where

$$\begin{aligned}
\mathcal{Z}_1 &= 2\sqrt{3}\eta^2 r^3\left(6\eta M+r^3\right)^2\left(\frac{\left(L^2+r^2\right)\left(3\eta-r^2\log\left(\frac{6\eta M}{r^3}+1\right)\right)}{\eta}\right)^{3/2},\\
\mathcal{Z}_2 &= r^4\left(6\eta M+r^3\right)^2\log\left(\frac{6\eta M}{r^3}+1\right)-9\eta(L^2(-6\eta M^2\left(r^2-6\eta\right)\\
&\quad -4M\left(r^5-3\eta r^3\right)+r^6)+18\eta M^2r^4),\\
\mathcal{Z}_3 &= \left(3\eta-r^2\log\left(\frac{6\eta M}{r^3}+1\right)\right),\\
\mathcal{Z}_4 &= \left(3\eta L^2\left(6\eta M-3Mr^2+r^3\right)-9\eta Mr^4+r^4\left(6\eta M+r^3\right)\log\left(\frac{6\eta M}{r^3}+1\right)\right)^2.
\end{aligned}$$

For vanishing black hole parameters $\eta = 0$, equations (3.31)-(3.32) simplify to the radial, latitudinal, and axial frequencies of test particles in the vicinity of a Schwarzschild black hole. Equations (3.32) and (3.32) clearly indicate $\omega_\theta = \omega_\phi$.

Frequencies measured by distant observer

The locally defined angular frequencies ω_β are delineated in Eqs. ((3.31)-(3.32)). Conversely, the angular frequencies observed by a stationary distant observer (Ω) are expressed as:

$$\Omega_\beta = \omega_\beta\frac{d\tau}{dt}, \tag{3.33}$$

where $\dot{\tau}/\dot{t}$ is the redshift coefficient, given by

$$\frac{dt}{d\tau} = -\frac{\mathcal{E}}{g_{tt}}. \tag{3.34}$$

When a distant observer measures the frequencies of minor harmonic oscillations in physical units, the frequencies of neutral particles, as ascertained by these observers, assume the following form

$$\nu_i = \frac{1}{2\pi}\frac{c^3}{GM}\,\Omega_i[\mathrm{Hz}], \tag{3.35}$$

where $i \in \{r, \theta, \phi\}$; Ω_r, Ω_θ, and Ω_ϕ denotes the dimensionless radial, latitudinal, and axial angular frequencies measured by a distant observer, given by

$$\begin{aligned}\Omega_r^2 &= \frac{27\eta\left(12\eta+(r-4)r^2\right)}{3\eta\left(6\eta+r^3\right)^2} \\ &+ \frac{\left(-144\eta^2-4r^6+15r^5-48\eta r^3+36\eta r^2\right)\log\left(\frac{6\eta}{r^3}+1\right)}{3\eta\left(6\eta+r^3\right)^2}, \qquad (3.36)\\ \Omega_\theta^2 &= \Omega_\phi^2 = \frac{3}{6\eta+r^3}-\frac{\log\left(\frac{6\eta}{r^3}+1\right)}{3\eta}, \qquad (3.37)\end{aligned}$$

The radial profiles of frequencies ν_j, detected by a distant observer, for small harmonic oscillations of neutral particles around non-rotating regular BHs within asymptotically safe gravity for different values of BH parameter η are shown in Figure 3.5. The radial profiles for the orbital frequency (Ω_ϕ) and the latitudinal frequency (Ω_θ) coincide, which is a typical behavior for the frequencies of particles around non-rotating BHs. The BH parameter η contributes to the shift in the fundamental frequencies of the test particles close to the BH horizon. The particles around Schwarzschild BH have higher frequencies as compared to those particles traveling around regular BH within asymptotically safe gravity.

Periastron precession

This section addresses the periastron frequency of a neutral test particle orbiting a non-rotating regular black hole within the framework of asymptotically safe gravity, considering the limit of a little perturbation relative to the equatorial

plane at $\pi/2$. To compute the Periastron precession, we suppose that the particle is minimally disturbed from its stable location, leading to oscillations around that point with a radial frequency Ω_r. The periastron frequency Ω_P is defined as the difference between the orbital frequency Ω_ϕ and the radial frequency Ω_r, expressed by the relation

$$\Omega_P = \Omega_\phi - \Omega_r, \tag{3.38}$$

$$\Omega_P = \sqrt{\frac{3M}{6\eta M + r^3} - \frac{\ln\left(\frac{6\eta M}{r^3}+1\right)}{3\eta}} - \frac{\sqrt{\frac{P_1}{P_2}}}{\sqrt{3}}, \tag{3.39}$$

where

$$\begin{aligned} P_1 &= \left(36\eta M^2\left(r^2-4\eta\right)+3M\left(5r^5-16\eta r^3\right)\right. \\ &\quad \left.-4r^6\right)\ln\left(\frac{6\eta M}{r^3}+1\right)+27\eta M\left(r^3-4M\left(r^2-3\eta\right)\right), \\ P_2 &= \eta\left(6\eta M+r^3\right)^2. \end{aligned}$$

The graphical behavior of periastron frequency for particles orbiting a non-rotating regular black hole within the framework of asymptotically safe gravity is illustrated in Fig. 3.6. The frequency of the periastron is shown to decrease with an increase in the parameter η and likewise decrease with increasing radial distance r.

3.5 Relativistic Precession Model

The relativistic precession (RP) model [113, 114] is one of the most widely used frameworks for explaining quasi-periodic oscillations (QPOs) observed in X-ray binaries. While the RP model was originally developed for Kerr black holes, it relies only on orbital and epicyclic frequencies, which exist in any stationary space-time. In the non-rotating spherical limit, the model remains valid as relativistic periastron precession persists even in the absence of spin. This model attributes

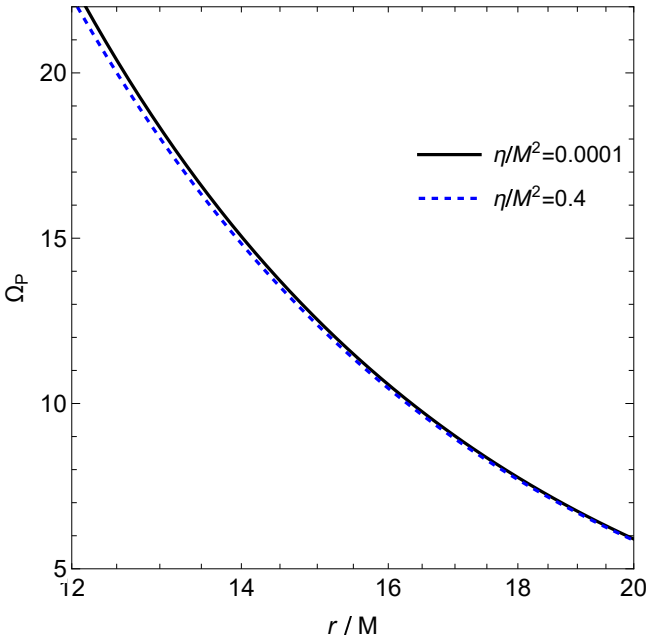

Figure 3.6: Periastron frequency of particles in the background of regular BHs within asymptotically safe gravity, for varying values of BH parameter η.

QPO frequencies to the fundamental oscillatory motion of matter in the strong gravitational field of a compact object, such as a black hole. Specifically, it links observed QPO frequencies to the orbital, radial, and vertical epicyclic motion of matter within an accretion disk.

In the RP model, the three key frequencies are:

- **Orbital frequency** (ν_ϕ): The Keplerian frequency at which a particle orbits the compact object.

- **Radial epicyclic frequency** (ν_r): The frequency of small radial perturbations around the circular orbit.

- **Vertical epicyclic frequency** (ν_θ): The frequency of small vertical perturbations around the orbital plane.

The twin-peak QPOs observed in many X-ray binaries are interpreted within

the RP model as follows:

$$\nu_U = \nu_\phi, \quad \text{(Upper QPO frequency)} \tag{3.40}$$

$$\nu_L = \nu_\phi - \nu_r. \quad \text{(Lower QPO frequency)} \tag{3.41}$$

This model naturally explains the observed 3:2 frequency ratio in high-frequency QPOs (HFQPOs) as a resonance condition between these fundamental oscillatory modes [115, 116].

Application to the asymptotically safe gravity

In our study, we apply the RP model to the asymptotically safe gravity, where the presence of the parameter η modifies the orbital and epicyclic frequencies. The effect of η on QPO frequencies is crucial for understanding observational constraints on this parameter.

Figure 3.7 illustrates the variation of the upper and lower QPO frequencies as functions of r/M for different values of η. Notably, the 3:2 resonance occurs at different radii depending on η, which implies that the parameter influences the possible locations where QPOs can be detected.

Figure 3.8 shows the relationship between the upper and lower QPO frequencies for various values of η. The modification in this relationship compared to the standard RP model suggests that future X-ray observations could potentially constrain η by identifying deviations from the expected Schwarzschild predictions.

The $\nu_U/\nu_L \approx 3/2$ condition allows us to determine r as a function of the black hole mass. Figure 3.9 illustrates the relationship between the lower frequency and r, with results derived from this condition, alongside selected datasets. As mentioned, the spacetime parameter must lie within its maximum and minimum values, which are indicated by the shaded region. This implies that the spacetime

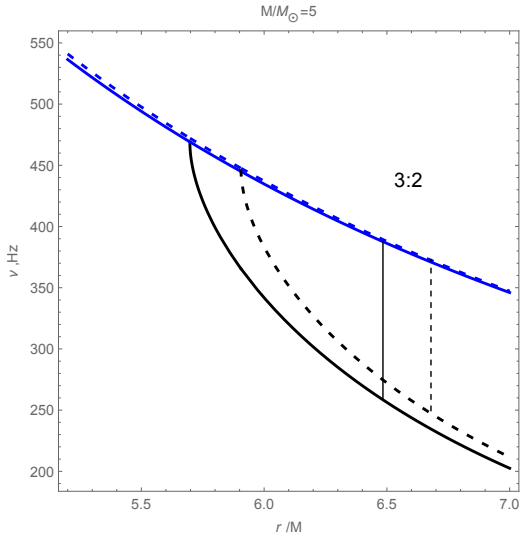

Figure 3.7: The radial profile of the upper (ν_U , blue) and lower (ν_L, black) frequencies is presented for the RP model. The panel displays results for two distinct values of η/M^2 (solid lines for $\eta/M^2 = 0.3$, while dashed lines for $\eta/M^2 = 0.1$). Furthermore, $r_{3:2}$ resonance radii are also displayed by solid and dashed vertical lines.

model can only account for the data within this shaded area. From Figure 3.9, only two data points are available; however, since GRS 1915+105 corresponds to a rotating case, it cannot be used in this analysis. Additionally, the figure provides prior values(3.2) for the Markov Chain Monte Carlo (MCMC) analysis.

3.6 Constraints on the mass of a asymptotically safe black hole

This section examines X-ray binary systems to provide limitations on the parameters of our considered black hole model. This entails analyzing QPOs data from these systems, focusing on source H1743-322. We will ultimately present the optimal parameter values obtained via Markov Chain Monte Carlo (MCMC) research. The MCMC analysis was performed with the Python package 'emcee' [117], with the objective of establishing constraints on the black hole parameters

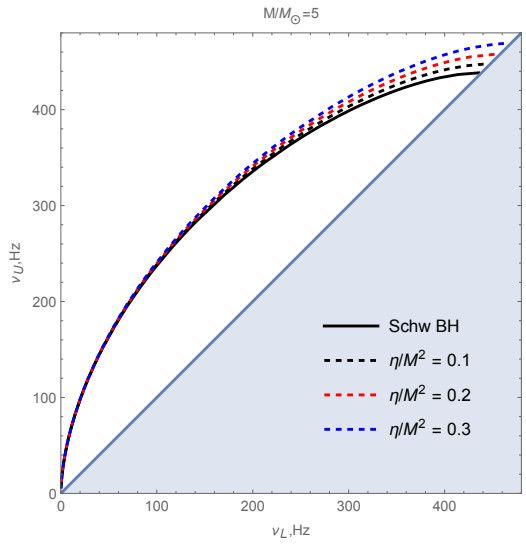

Figure 3.8: The relationships between the frequencies of the upper and lower peaks of the twin-peak QPOs in the RP model are investigated around a BH of asymptotical safe gravity with a mass of $M = 5M_{\odot}$.

derived from the relativistic precession (RP) model. The posterior distribution is delineated as specified in [118]:

$$\mathcal{P}(\Theta|D,M) = \frac{P(D|\Theta,M)\pi(\Theta|M)}{P(D|M)},$$

where: - $\pi(\Theta)$ represents the prior distribution, - $P(D|\Theta,M)$ is the likelihood. The priors are Gaussian within set boundaries:

$$\pi(\Theta_i) \sim \exp\left(-\frac{1}{2\sigma_i^2}(\Theta_i - \Theta_0)^2\right),$$

subject to $\Theta_{\text{low},i} < \Theta_i < \Theta_{\text{high},i}$ for the parameters $\Theta_i = [M, r/M, \eta/M^2]$, where σ_i are their standard deviations. We use η/M^2 and $r = r_{3:2}/M$ to denote the normalized radial location of the 3:2 resonance. Table 3.2 lists the prior values for the parameters of the safe gravity [119–123].

Incorporating the upper and lower frequency data obtained in Fig.3.8 by Eq. (3.7), our MCMC analysis utilizes two distinct datasets. Central to this analysis is the likelihood function, $\mathcal{L}$, which is formulated as:

Table 3.1: The mass, upper and lower frequencies of QPOs from the X-ray binaries selected for analysis.

	H1743-322
$M(M_{\odot})$	$\leq$9.78 [124]
ν_{up}(Hz)	240Â±3 [124]
ν_{low}(Hz)	165^{+9}_{-5} [124]

$$\log \mathcal{L} = \log \mathcal{L}_{\rm up} + \log \mathcal{L}_{\rm low}.$$

This means that the logarithm of the likelihood function is expressed as the sum of the logarithms of the likelihoods for the upper and lower frequency datasets. Specifically, $\log \mathcal{L}_{\rm up}$ represents the likelihood associated with the upper frequency data and is given by:

$$\log \mathcal{L}_{\rm up} = -\frac{1}{2} \sum_i \left(\frac{(\nu^i_{\rm up,\ obs} - \nu^i_{\rm up,\ th})^2}{(\sigma^i_{\rm up,\ obs})^2} \right).$$

Similarly, $\log \mathcal{L}_{\rm low}$ denotes the likelihood related to the lower frequency data, formulated as:

$$\log \mathcal{L}_{\rm low} = -\frac{1}{2} \sum_i \left(\frac{(\nu^i_{\rm low,\ obs} - \nu^i_{\rm low,\ th})^2}{(\sigma^i_{\rm low,\ obs})^2} \right)$$

Here, i indexes the upper and lower frequencies measured. The upper and lower frequencies observed are denoted $\nu^i_{\rm up,\ obs}$ and $\nu^i_{\rm low,\ obs}$, while $\nu^i_{\rm up,\ th}$ and $\nu^i_{\rm low,\ th}$ refer to their theoretical counterparts. The terms $\sigma^i_{\rm up}$ and $\sigma^i_{\rm low}$ indicate the statistical uncertainties of these values.

Table 3.2: The Gaussian prior of the BHs within asymptotically safe gravity derived from QPOs for the selected X-ray sources.

Parameters	H1743-322
$M(M_\odot)$	8.2 ± 0.25
r/M	6.5 ± 0.2
η/M^2	0.25 ± 0.012

Table 3.3: The best-fit parameter values resembling those of BHs within asymptotically safe gravity, deduced from the QPOs for the chosen X-ray sources.

Parameters	H1743-322
$M(M_\odot)$	8.16 ± 0.17
r/M	$6.44^{+0.08}_{-0.07}$
η/M^2	0.25 ± 0.02

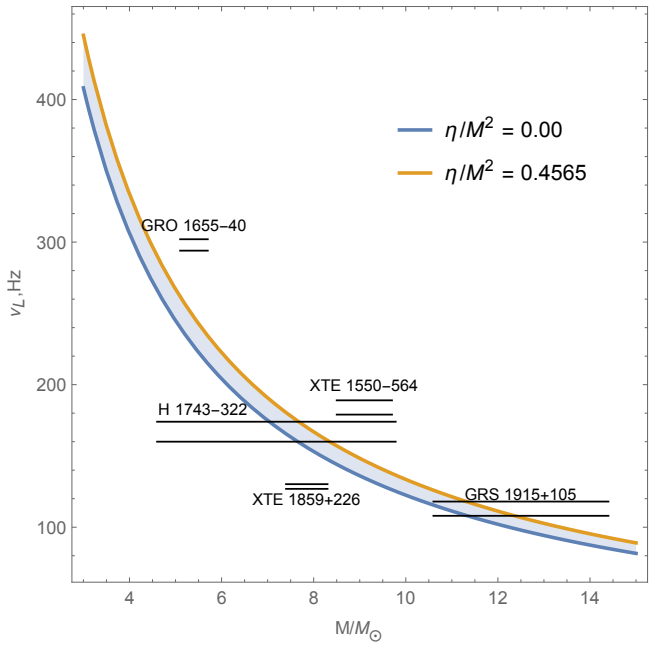

Figure 3.9: The lower frequency as a function of the black hole mass (measured in solar mass units).

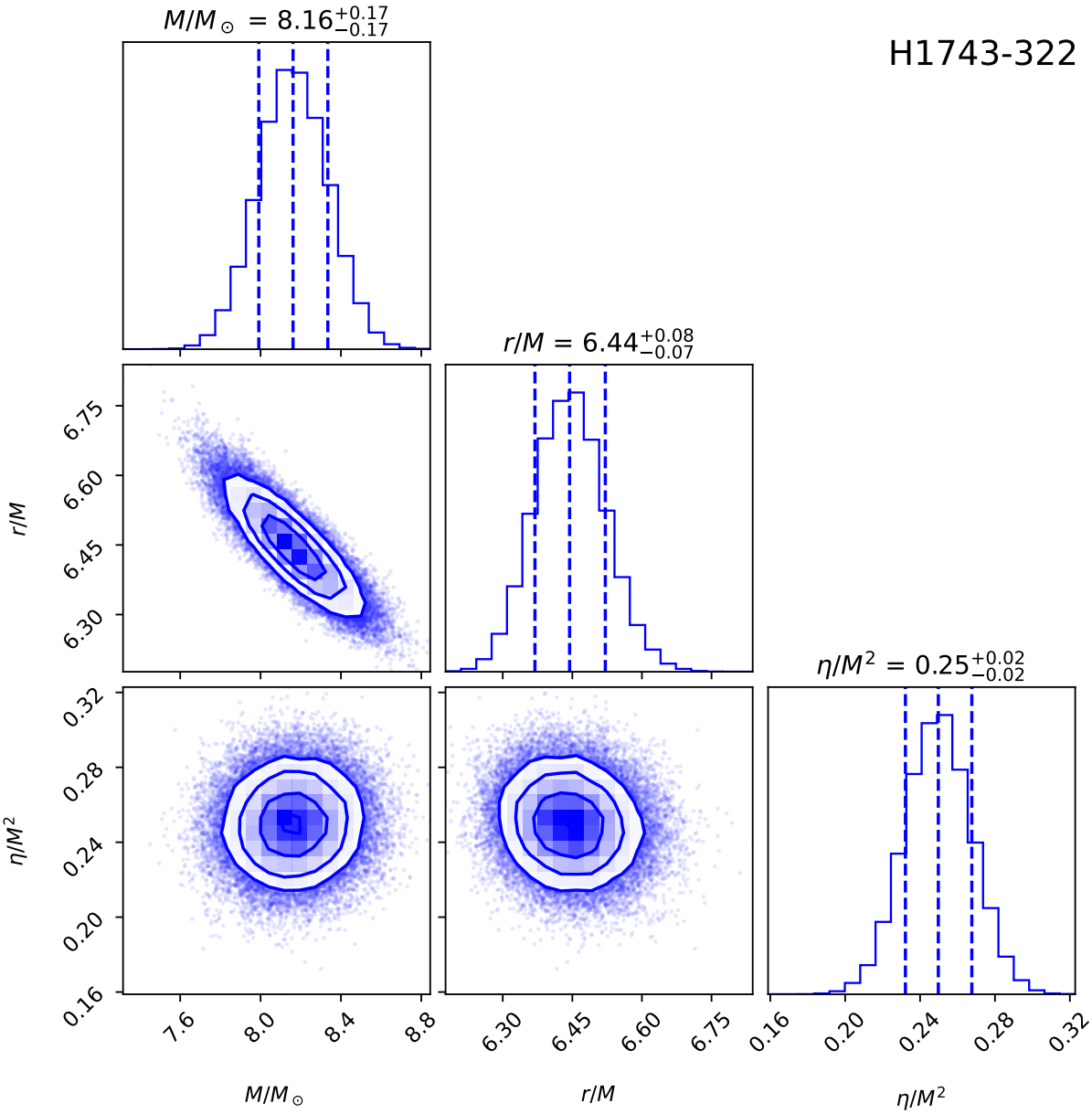

Figure 3.10: Constraints on BHs mass within asymptotically safe gravity, the η parameter in the microquasar H1743-322 using MCMC code.

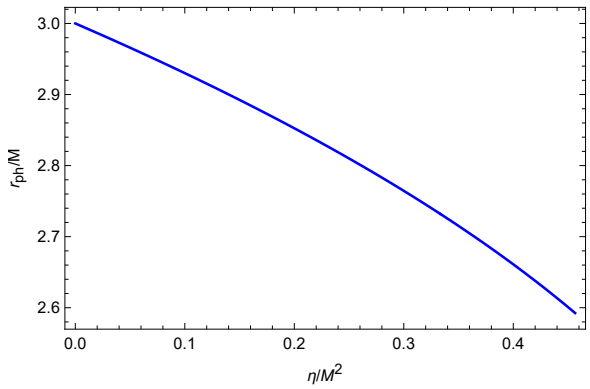

Figure 3.11: Dependence of the photon sphere radius on the parameter η/M^2.

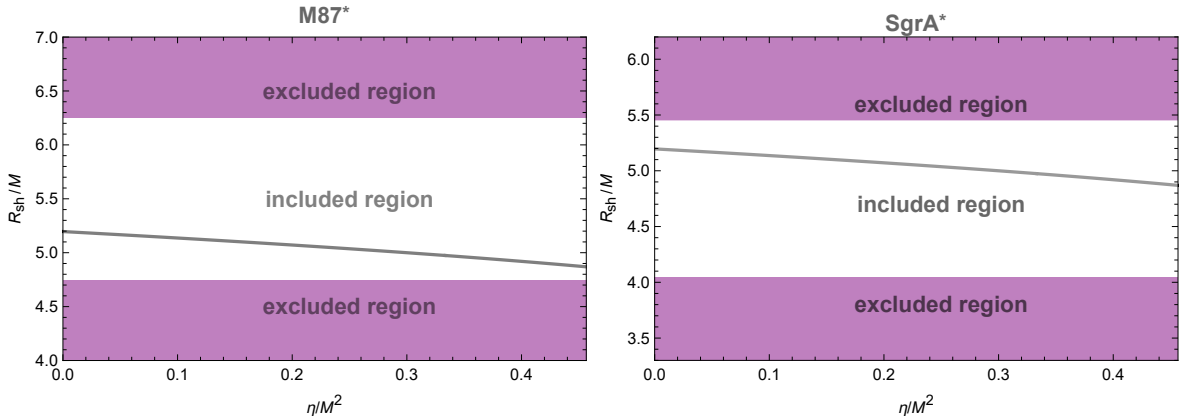

Figure 3.12: The radius of shadow for regular BH within the asymptotically safe gravity as a function of parameter η/M^2 for M87* (left panel) and for Sgr A* (right panel).

3.7 Black hole shadow with M87* and Sgr A*

This section examines the shadow of the regular black hole in the background of asymptotically safe gravity. A geometry-based method determines the angular radius α of the black hole's shadow [53, 55]

$$\sin^2 \alpha_{sh} = \frac{h^2(r_{ph})}{h^2(r_o)}, \tag{3.42}$$

where

$$h^2(r_{ph}) = \frac{r_{ph}^2}{f(r_{ph})}, \quad h^2(r_o) = \frac{r_o^2}{f(r_o)}. \tag{3.43}$$

The position of the observer is represented by r_o, whereas the photon sphere radius r_{ph} is determined by the following equation.

$$\frac{\mathrm{d}(h^2(r))}{\mathrm{d}r}\Big|_{r=r_{ph}} = 0. \tag{3.44}$$

By placing the observer at quite a distance from the black hole and using Eqs. 3.42 and 3.43 we can get an approximate formula for the radius of the black hole's shadow as [53, 55]

$$R_{sh} \approx r_0 \sin \alpha_{sh} = \sqrt{r_p^2 \frac{1}{f(r_p)}}. \tag{3.45}$$

Fig. 3.11 shows the dependence of the photon sphere radius on the parameter η/M^2. We can see from the graph that photon sphere radius decreases as parameter η/M^2 increase. Now we consider the supermassive BHs M87 and Sgr A to be regular black holes in the background of asymptotically safe gravity. We employ observational data supplied by the EHT project for the BH shadows of the supermassive BHs M87* and Sgr A*, therefore constraining this parameter η in the background of safe gravity. The angular diameter of the shadow, the distance from the solar system, and the mass of the BH at the center of the galaxy M87 are $\Omega_{\mathrm{M87}^*} = 42 \pm 3\ \mu$as, $D = 16.8 \pm 0.8$ Mpc and $M_{\mathrm{M87}^*} = (6.5 \pm 0.7)\mathrm{x}10^9\ M_\odot$

respectively [83]. Data recently acquired by the EHT project for the $\Omega_{\text{Sgr A}^*} = 48.7 \pm 7 \mu$as, $D = 8277 \pm 9 \pm 33$ pc and $M_{\text{Sgr A}^*} = 4.297 \pm 0.013\text{x}10^6 M_\odot$ (VLTI) [2]. We can now derive the diameter of the shadow using the calculation $d_{\text{sh}}^{\text{theo}} = 2R_{\text{sh}}$. The diameter of the black hole shadow image is $d_{\text{sh}}^{\text{M87}^*} = (11 \pm 1.5)M$ for M87* and $d_{\text{sh}}^{\text{Sgr A}^*} = (9.5 \pm 1.4)M$ for Sgr A*. Based on the data from the EHT collaboration, we derive the constraint on the parameter η for the supermassive black holes at the centers of galaxies M87* and Sgr A*. We provide our findings illustrated in Fig. 3.12. The image illustrates that the radius of the black hole shadow decreases as the parameter η increases. It is clear from the graph that the values $0 < \eta/M^2 < 0.4565$ are in complete agreement with the EHT observations for M87* and SgrA*. In the range $\eta/M^2 > 0.4565$, the spacetime no longer possesses horizons, indicating the presence of a horizonless compact object characterized by two photon rings [125].

3.8 Conclusion

We have explored the circular motion of neutral test particles around non-rotating regular BH within asymptotically safe gravity and investigated the effects of parameters of the BH on the particle's motion. We have discussed the stability of equatorial circular orbits using the effective potential approach. The behavior of the effective potential is shown for different values of the BH parameter η, and for different values of the angular momentum $\mathcal{L}$ for $\eta < \eta_{cr}$ and $\eta = \eta_{cr}$. The unstable and stable circular orbits, respectively, correspond to the maximum and minimum effective potentials. When $\eta < \eta_{cr}$, the effective potential does not increase much as we increase the values of angular momentum. It is interesting to note that both the BH parameter η and the particle's angular momentum $\mathcal{L}$ behave similarly on effective potential. The effective potential increases with increasing either the BH

parameter η or the angular momentum of the particle $\mathcal{L}$. It is noted that when the particles travel close to the event horizon of BH, the circular orbits are stable, and stability decreases as we particles move away from the BH.

We have obtained the analytical expressions for energy and angular momentum of equatorial circular orbits around non-rotating regular BH within asymptotically safe gravity, as a function of BH parameters. It is noted that when the value of the BH parameter η is small, the particles have a high energy; however, the energy decreases for large values of η. Furthermore, the energy increases monotonically as the radial distance r increases. We have shown the behavior of the angular momentum as a function of r for varying values of the BH parameter η. It is shown that when the value of the BH parameter η is small, the particles have a large angular momentum, while the particles have a small angular momentum for increasing values of the BH parameter η. However, the angular momentum increases monotonically as the radial distance r increases.

We have explored the epicyclic oscillations and fundamental frequencies of test particles moving around a regular BH within asymptotically safe gravity. The BH parameter η is shown to contribute to the shift of the fundamental frequencies of the test particles close to the BH horizon. The particles around Schwarzschild BH have higher frequencies as compared to those particles traveling around regular BH within asymptotically safe gravity. We also examine the frequency of the periastron and the effects of the BH parameter on it. We observed that the frequency of the periastron decreases as the parameter η increases and also decreases with increasing radial distance r.

Also, we have studied the radius of photon sphere and shadow of the regular black hole in the background of asymptotically safe gravity. Our analysis confirms that an increase in the parameter η leads to a decrease in both the photon sphere

radius and the shadow radius. Using EHT collaboration data, we obtained a constraint on the parameter η for the supermassive black hole Sgr A* and M87*. Consequently, the regular BH parameter η has been constrained to $0 < \eta/M^2 < 0.4565$ for both Sgr A* and M87*.

Conclusion

The following conclusions were presented based on research carried out on the topic of "Optical Properties and Dynamics of Particles Around Black Holes in Modified Gravities" for the Doctor of Philosophy (PhD) dissertation:

1. It has been obtained that the equations of motion for spinning particles around quantum-corrected black holes reveal a significant dependence of the effective potential, ISCO radius, and superluminal bounds on both spin and quantum gravity parameters.

2. It has been obtained that the optical properties of Reissner–Nordström-like black holes in Kalb–Ramond gravity are strongly affected by Lorentz-violating parameters and plasma distributions, and it has been shown how these factors influence the photon sphere and shadow radius.

3. It has been demonstrated that theoretical predictions of black hole shadow sizes, when compared with Event Horizon Telescope observations of Sgr A* and M87*, allow for the establishment of constraints on parameters in modified gravity theories.

4. It has been shown that regular black holes in asymptotically safe gravity exhibit distinct astrophysical and orbital properties, including characteristic epicyclic oscillations and precession effects, with potential observational signatures.

Bibliography

[1] K. Akiyama and et al., "First M87 Event Horizon Telescope Results. I. The Shadow of the Supermassive Black Hole," *ApJ.*, vol. 875, no. 1, p. L1, Apr. 2019.

[2] K. Akiyama and et al., "First Sagittarius A* Event Horizon Telescope Results. I. The Shadow of the Supermassive Black Hole in the Center of the Milky Way," *Astrophys. J. Lett*, vol. 930, no. 2, p. L12, May 2022.

[3] B. P. Abbott and et al., "Tests of general relativity with the binary black hole signals from the LIGO-Virgo catalog GWTC-1," *Phys. Rev. D*, vol. 100, no. 10, p. 104036, Nov. 2019.

[4] T. Johannsen and D. Psaltis, "Metric for rapidly spinning black holes suitable for strong-field tests of the no-hair theorem," *Phys. Rev. D*, vol. 83, p. 124015, Jun 2011. [Online]. Available: https://link.aps.org/doi/10.1103/PhysRevD.83.124015

[5] L. Rezzolla and A. Zhidenko, "New parametrization for spherically symmetric black holes in metric theories of gravity," *Phys. Rev. D*, vol. 90, p. 084009, Oct 2014. [Online]. Available: https://link.aps.org/doi/10.1103/PhysRevD.90.084009

[6] R. Konoplya, L. Rezzolla, and A. Zhidenko, "General parametrization of axisymmetric black holes in metric theories of gravity," *Phys. Rev. D*, vol. 93, p. 064015, Mar 2016. [Online]. Available: https://link.aps.org/doi/10.1103/PhysRevD.93.064015

[7] R. Ruffini and J. A. Wheeler, "Introducing the black hole," *Physics Today*, vol. 24, no. 1, p. 30, Jan. 1971.

[8] S. W. Hawking, "Black holes in general relativity," *Communications in Mathematical Physics*, vol. 25, no. 2, pp. 152–166, Jun. 1972.

[9] S. W. Hawking, M. J. Perry, and A. Strominger, "Soft Hair on Black Holes," *Phys. Rev. Lett.*, vol. 116, no. 23, p. 231301, Jun. 2016.

[10] J. Ovalle, R. Casadio, E. Contreras, and A. Sotomayor, "Hairy black holes by gravitational decoupling," *Physics of the Dark Universe*, vol. 31, p. 100744, Jan. 2021.

[11] C. Martínez, R. Troncoso, and J. Zanelli, "Exact black hole solution with a minimally coupled scalar field," *Phys. Rev. D*, vol. 70, no. 8, p. 084035, Oct. 2004.

[12] C. A. R. Herdeiro and E. Radu, "Asymptotically flat black holes with scalar hair: A review," *Int. J. Mod. Phys. D*, vol. 24, no. 9, pp. 1 542 014–219, Jun. 2015.

[13] R. M. Plyatsko, O. B. Stefanyshyn, and M. T. Fenyk, "Mathisson-Papapetrou-Dixon equations in the Schwarzschild and Kerr backgrounds," *Classical and Quantum Gravity*, vol. 28, no. 19, p. 195025, Oct. 2011.

[14] M. Mathisson, "Neue mechanik materieller systemes," *Acta Phys. Polon.*, vol. 6, pp. 163–2900, 1937.

[15] A. Papapetrou, "Spinning test particles in general relativity. 1." *Proc. Roy. Soc. Lond. A*, vol. 209, pp. 248–258, 1951.

[16] E. Corinaldesi and A. Papapetrou, "Spinning test particles in general relativity. 2." *Proc. Roy. Soc. Lond. A*, vol. 209, pp. 259–268, 1951.

[17] J. Lewandowski, Y. Ma, J. Yang, and C. Zhang, "Quantum Oppenheimer-Snyder and Swiss Cheese Models," *Phys. Rev. Lett.*, vol. 130, no. 10, p. 101501, Mar. 2023.

[18] S. Yang, Y.-P. Zhang, T. Zhu, L. Zhao, and Y.-X. Liu, "Gravitational waveforms from periodic orbits around a quantum-corrected black hole," *J. Cosmol. Astropart. Phys.*, vol. 2025, no. 1, p. 091, Jan. 2025.

[19] C. Rovelli, *Quantum Gravity*, ser. Cambridge Monographs on Mathematical Physics. Cambridge, UK: Cambridge University Press, 2004. [Online]. Available: https://www.cambridge.org/core/books/quantum-gravity/2CE80F4FA41907B45B22E16E14EBD168

[20] F. Abdulxamidov, J. Rayimbaev, A. Abdujabbarov, and Z. c. v. Stuchlík, "Spinning magnetized particles orbiting magnetized schwarzschild black holes," *Phys. Rev. D*, vol. 108, p. 044030, Aug 2023. [Online]. Available: https://link.aps.org/doi/10.1103/PhysRevD.108.044030

[21] B. Toshmatov and D. Malafarina, "Spinning test particles in the γ spacetime," *Phys. Rev. D*, vol. 100, p. 104052, Nov 2019. [Online]. Available: https://link.aps.org/doi/10.1103/PhysRevD.100.104052

[22] F. Abdulxamidov, J. Rayimbaev, A. Abdujabbarov, and Z. Stuchlík, "Spinning magnetized particles orbiting magnetized Schwarzschild black holes," *Phys. Rev. D*, vol. 108, no. 4, p. 044030, 2023.

[23] B. Toshmatov and D. Malafarina, "Spinning test particles in the γ space-time," *Phys. Rev. D*, vol. 100, no. 10, p. 104052, Nov. 2019.

[24] K. Akiyama and et al. (Event Horizon Telescope Collaboration), "First M87 Event Horizon Telescope Results. I. The Shadow of the Supermassive Black Hole," *Astrophys. J.*, vol. 875, no. 1, p. L1, Apr 2019.

[25] ——, "First M87 Event Horizon Telescope Results. VI. The Shadow and Mass of the Central Black Hole," *Astrophys. J.*, vol. 875, no. 1, p. L6, Apr 2019.

[26] ——, "First Sagittarius A* Event Horizon Telescope Results. I. The Shadow of the Supermassive Black Hole in the Center of the Milky Way," *Astrophys. J.*, vol. 930, no. 2, p. L12, May 2022.

[27] F. W. Dyson, A. S. Eddington, and C. Davidson, "A Determination of the Deflection of Light by the Sun's Gravitational Field, from Observations Made at the Total Eclipse of May 29, 1919," *Philosophical Transactions of the Royal Society of London Series A*, vol. 220, pp. 291–333, Jan. 1920.

[28] B. P. Abbott and et al., "Observation of Gravitational Waves from a Binary Black Hole Merger," *Phys. Rev. Lett*, vol. 116, no. 6, p. 061102, Feb. 2016.

[29] B. Patla and R. J. Nemiroff, "Gravitational Lensing Characteristics of the Transparent Sun," *Astrophys. J*, vol. 685, no. 2, pp. 1297–1303, Oct. 2008.

[30] E. Berti and a. et, "Testing general relativity with present and future astrophysical observations," *Class. Quan. Grav.*, vol. 32, no. 24, p. 243001, Dec. 2015.

[31] C. Bambi, "Testing the space-time geometry around black hole candidates with the analysis of the broad Kα iron line," *Phys. Rev. D*, vol. 87, no. 2, p. 023007, Jan. 2013.

[32] K. G. Arun and A. Pai, "Tests of General Relativity and Alternative Theories of Gravity Using Gravitational Wave Observations," *International Journal of Modern Physics D*, vol. 22, no. 1, p. 1341012, Jan. 2013.

[33] J. Casanellas, P. Pani, I. Lopes, and V. Cardoso, "Testing Alternative Theories of Gravity Using the Sun," *Astrophys. J.*, vol. 745, no. 1, p. 15, Jan. 2012.

[34] B. Altschul, Q. G. Bailey, and V. A. Kostelecký, "Lorentz violation with an antisymmetric tensor," , vol. 81, no. 6, p. 065028, Mar. 2010.

[35] M. Kalb and P. Ramond, "Classical direct interstring action," , vol. 9, no. 8, pp. 2273–2284, Apr. 1974.

[36] W. F. Kao, W. B. Dai, S.-Y. Wang, T.-K. Chyi, and S.-Y. Lin, "Induced Einstein-Kalb-Ramond theory and the black hole," *Phys. Rev. D*, vol. 53, pp. 2244–2247, 1996.

[37] S. Chakraborty and S. SenGupta, "Strong gravitational lensing—a probe for extra dimensions and kalb-ramond field," *Journal of Cosmology and Astroparticle Physics*, vol. 2017, no. 07, p. 045, jul 2017. [Online]. Available: https://dx.doi.org/10.1088/1475-7516/2017/07/045

[38] K. K. Nair and M. T. Arun, "Kalb-Ramond field-induced cosmological bounce in generalized teleparallel gravity," , vol. 105, no. 10, p. 103505, May 2022.

[39] C.-E. Fu, Y.-X. Liu, K. Yang, and S.-W. Wei, "q-form fields on p-branes," *Journal of High Energy Physics*, vol. 2012, p. 60, Oct. 2012.

[40] S. Chakraborty and S. SenGupta, "Solutions on a brane in a bulk spacetime with Kalb-Ramond field," *Annals of Physics*, vol. 367, pp. 258–279, Apr. 2016.

[41] L. A. Lessa, J. E. G. Silva, R. V. Maluf, and C. A. S. Almeida, "Modified black hole solution with a background Kalb-Ramond field," *European Physical Journal C*, vol. 80, no. 4, p. 335, Apr. 2020.

[42] F. Atamurotov, D. Ortiqboev, A. Abdujabbarov, and G. Mustafa, "Particle dynamics and gravitational weak lensing around black hole in the Kalb-Ramond gravity," *Eur. Phys. J. C*, vol. 82, no. 8, p. 659, Aug. 2022.

[43] D. Ortiqboev, F. Javed, F. Atamurotov, A. Abdujabbarov, and G. Mustafa, "Energy extraction and Keplerian fundamental frequencies in the Kalb–Ramond gravity," *Phys. Dark Univ.*, vol. 46, p. 101615, Dec. 2024.

[44] A. Einstein, "Lens-Like Action of a Star by the Deviation of Light in the Gravitational Field," *Science*, vol. 84, no. 2188, pp. 506–507, Dec. 1936.

[45] P. Schneider, J. Ehlers, and E. E. Falco, *Gravitational Lenses*, 1992.

[46] J. L. Synge, "Classical dynamics," in *Principles of Classical Mechanics and Field Theory/Prinzipien der Klassischen Mechanik und Feldtheorie*. Springer, 1960, pp. 1–225.

[47] G. S. Bisnovatyi-Kogan and O. Y. Tsupko, "Gravitational radiospectrometer," *Gravitation and Cosmology*, vol. 15, no. 1, pp. 20–27, Mar. 2009.

[48] K. Yang, Y.-Z. Chen, Z.-Q. Duan, and J.-Y. Zhao, "Static and spherically symmetric black holes in gravity with a background Kalb-Ramond field," , vol. 108, no. 12, p. 124004, Dec. 2023.

[49] Z.-Q. Duan, J.-Y. Zhao, and K. Yang, "Electrically charged black holes in gravity with a background Kalb-Ramond field," *arXiv e-prints*, p. arXiv:2310.13555, Oct. 2023.

[50] J. L. Synge, *Relativity: The general theory*, nh ed. North Holland Publishing Co, 1960. [Online]. Available: http://gen.lib.rus.ec/book/index.php?md5=7ae08880cf8086fed4d3bcf732be8e54

[51] J. T. Mendonça, J. D. Rodrigues, and H. Terças, "Axion production in unstable magnetized plasmas," , vol. 101, no. 5, p. 051701, Mar. 2020.

[52] V. Perlick, O. Y. Tsupko, and G. S. Bisnovatyi-Kogan, "Influence of a plasma on the shadow of a spherically symmetric black hole," *Phys. Rev. D*, vol. 92, no. 10, p. 104031, Nov. 2015.

[53] V. Perlick and O. Y. Tsupko, "Calculating black hole shadows: Review of analytical studies," *Phys. Rep.*, vol. 947, pp. 1–39, Feb. 2022.

[54] A. Davlataliev, B. Narzilloev, I. Hussain, A. Abdujabbarov, and B. Ahmedov, "Probing the Starobinsky-Bel-Robinson gravity by photon motion around the Kerr-type black hole in non-uniform plasma," *Phys. Dark Univ.*, vol. 42, p. 101340, 2023.

[55] S. Vagnozzi and et al., "Horizon-scale tests of gravity theories and fundamental physics from the Event Horizon Telescope image of Sagittarius A (*)," *Classical and Quantum Gravity*, vol. 40, no. 16, p. 165007, Aug. 2023.

[56] K. Akiyama *et al.*, "First Sagittarius A* Event Horizon Telescope Results. I. The Shadow of the Supermassive Black Hole in the Center of the Milky Way," *Astrophys. J. Lett.*, vol. 930, no. 2, p. L12, 2022.

[57] G. S. Bisnovatyi-Kogan and O. Y. Tsupko, "Gravitational lensing in a non-uniform plasma," *Mon. Not. R. Astron. Soc*, vol. 404, pp. 1790–1800, Jun. 2010.

[58] G. Z. Babar, F. Atamurotov, and A. Z. Babar, "Gravitational lensing in 4-D Einstein-Gauss-Bonnet gravity in the presence of plasma," *Physics of the Dark Universe*, vol. 32, p. 100798, May 2021.

[59] K. S. Virbhadra and G. F. R. Ellis, "Schwarzschild black hole lensing," *Phys. Rev. D*, vol. 62, p. 084003, 2000.

[60] K. S. Virbhadra, "Relativistic images of Schwarzschild black hole lensing," *Phys. Rev. D*, vol. 79, no. 8, p. 083004, Apr. 2009.

[61] V. Bozza, "Gravitational Lensing by Black Holes," *Gen. Rel. Grav.*, vol. 42, pp. 2269–2300, 2010.

[62] A. Younas, S. Hussain, M. Jamil, and S. Bahamonde, "Strong Gravitational Lensing by Kiselev Black Hole," *Phys. Rev. D*, vol. 92, no. 8, p. 084042, 2015.

[63] M. Azreg-Aïnou, S. Bahamonde, and M. Jamil, "Strong Gravitational Lensing by a Charged Kiselev Black Hole," *Eur. Phys. J. C*, vol. 77, no. 6, p. 414, 2017.

[64] Z. Turakhonov, F. Atamurotov, A. Ovgun, A. Abdujabbarov, and S. Urinov, "Weak gravitational lensing around dyonic modmax black hole in plasma," *Communications in Theoretical Physics*, 2024. [Online]. Available: http://iopscience.iop.org/article/10.1088/1572-9494/ad6853

[65] B. Turimov, B. Ahmedov, A. Abdujabbarov, and C. Bambi, "Gravitational lensing by a magnetized compact object in the presence of plasma," *Inter-*

national Journal of Modern Physics D, vol. 28, no. 16, pp. 2 040 013–187, Jan. 2019.

[66] J. Bardeen, "Non-singular general relativistic gravitational collapse," in *Proceedings of the 5th International Conference on Gravitation and the Theory of Relativity*, Sep. 1968, p. 87.

[67] E. Ayón-Beato and A. García, "Regular Black Hole in General Relativity Coupled to Nonlinear Electrodynamics," *Phys. Rev. Lett.*, vol. 80, no. 23, pp. 5056–5059, Jun. 1998.

[68] S. A. Hayward, "Formation and Evaporation of Nonsingular Black Holes," *Phys. Rev. Lett.*, vol. 96, no. 3, p. 031103, Jan. 2006.

[69] Z.-Y. Fan and X. Wang, "Construction of regular black holes in general relativity," *Phys. Rev. D*, vol. 94, no. 12, p. 124027, Dec. 2016.

[70] A. Davlataliev, B. Narzilloev, I. Hussain, A. Abdujabbarov, and B. Ahmedov, "Long-lived quasinormal modes and asymptotic tails of regular Schwarzschild-like black holes in the presence of a magnetic field," 12 2024.

[71] J. Ovalle, R. Casadio, and A. Giusti, "Regular hairy black holes through Minkowski deformation," *Phys. Lett. B*, vol. 844, p. 138085, Sep. 2023.

[72] J. T. S. S. Junior, F. S. N. Lobo, and M. E. Rodrigues, "(Regular) Black holes in conformal Killing gravity coupled to nonlinear electrodynamics and scalar fields," *Class. Quant. Grav.*, vol. 41, no. 5, p. 055012, Mar. 2024.

[73] A. Bakopoulos, C. Charmousis, P. Kanti, N. Lecoeur, and T. Nakas, "Black holes with primary scalar hair," *Phys. Rev. D*, vol. 109, no. 2, p. 024032, Jan. 2024.

[74] B. Turimov, A. Davlataliev, Y. Usmanov, S. Karshiboev, and P. Tadjimuratov, "Investigating new aspects of Bocharova–Bronnikov–Melnikov–Bekenstein spacetime: ionized thin accretion disk model," *Eur. Phys. J. C*, vol. 84, no. 10, p. 1098, 2024.

[75] B. Turimov, A. Davlataliev, B. Ahmedov, and Z. Stuchlík, "Exploring a novel feature of ellis spacetime: Insights into scalar field dynamics," *Chin. J. Phys.*, vol. 94, pp. 807–819, 2025.

[76] B. Turimov, A. Davlataliev, A. Abdujabbarov, and B. Ahmedov, "Influence of scalar field in massive particle motion in JNW spacetime," *Phys. Rev. D*, vol. 110, no. 8, p. 084053, 2024.

[77] C. G. Böhmer and K. Vandersloot, "Loop quantum dynamics of the Schwarzschild interior," *Phys. Rev. D*, vol. 76, no. 10, p. 104030, Nov. 2007.

[78] L. Modesto and P. Nicolini, "Charged rotating noncommutative black holes," *Phys. Rev. D*, vol. 82, no. 10, p. 104035, Nov. 2010.

[79] A. Bonanno, D. Malafarina, and A. Panassiti, "Dust Collapse in Asymptotic Safety: A Path to Regular Black Holes," *Phys. Rev. Lett.*, vol. 132, no. 3, p. 031401, Jan. 2024.

[80] R. Carballo-Rubio, F. Di Filippo, S. Liberati, and M. Visser, "Geodesically complete black holes," *Phys. Rev. D*, vol. 101, no. 8, p. 084047, Apr. 2020.

[81] A. Bonanno and M. Reuter, "Renormalization group improved black hole spacetimes," *Phys. Rev. D*, vol. 62, no. 4, p. 043008, Aug. 2000.

[82] A. Bonanno, D. Malafarina, and A. Panassiti, "Dust Collapse in Asymptotic Safety: A Path to Regular Black Holes," *Phys. Rev. Lett.*, vol. 132, no. 3, p. 031401, Jan. 2024.

[83] K. Akiyama and et al. (Event Horizon Telescope Collaboration), "First M87 Event Horizon Telescope Results. I. The Shadow of the Supermassive Black Hole," *Astrophys. J.*, vol. 875, no. 1, p. L1, Apr 2019.

[84] B. P. Abbott and et al., "Observation of gravitational waves from a binary black hole merger," *Phys. Rev. Lett.*, vol. 116, p. 061102, Feb 2016. [Online]. Available: https://link.aps.org/doi/10.1103/PhysRevLett.116.061102

[85] K. G. Arun and a. et, "New horizons for fundamental physics with LISA," *Living Reviews in Relativity*, vol. 25, no. 1, p. 4, Dec. 2022.

[86] A. Flachi and J. P. S. Lemos, "Quasinormal modes of regular black holes," *Phys. Rev. D*, vol. 87, no. 2, p. 024034, Jan. 2013.

[87] S. Sau and J. W. Moffat, "Shadow of a regular black hole in scalar-tensor-vector gravity theory," *Phys. Rev. D*, vol. 107, no. 12, p. 124003, Jun. 2023.

[88] M. Kološ, M. Shahzadi, and Z. Stuchlík, "Quasi-periodic oscillations around Kerr-MOG black holes," *Eur. Phys. J. C*, vol. 80, no. 2, p. 133, Feb. 2020.

[89] M. Kološ, M. Shahzadi, and A. Tursunov, "Charged particle dynamics in parabolic magnetosphere around Schwarzschild black hole," *Eur. Phys. J. C*, vol. 83, no. 4, p. 323, Apr. 2023.

[90] M. Shahzadi, M. Kološ, R. Saleem, Y. Habib, and A. Eduarte-Rojas, "Structure-preserving numerical simulations of test particle dynamics around slowly rotating neutron stars within the Hartle-Thorne approach," *Phys. Rev. D*, vol. 108, no. 10, p. 103006, Nov. 2023.

[91] M. Kološ and M. Shahzadi, "Charged particles on resonant orbits around Schwarzschild black hole," in *Proceedings of RAGtime 23-25: Workshops*

on Black Holes and Neutron Stars, Z. Stuchlik, G. Torok, V. Karas, and D. Lancova, Eds., Jan. 2023, pp. 21–27.

[92] M. Shahzadi, M. Kološ, Z. Stuchlík, and Y. Habib, "Epicyclic oscillations in spinning particle motion around Kerr black hole applied in models fitting the quasi-periodic oscillations observed in microquasars and AGNs," *Eur. Phys. J. C*, vol. 81, no. 12, p. 1067, Dec. 2021.

[93] ——, "Testing alternative theories of gravity by fitting the hot-spot data of Sgr A*," *Eur. Phys. J. C*, vol. 82, no. 5, p. 407, May 2022.

[94] M. Shahzadi, M. Kološ, R. Saleem, and Z. Stuchlík, "Testing alternative spacetimes by high-frequency quasi-periodic oscillations observed in microquasars and active galactic nuclei," *Class. Quant. Grav.*, vol. 41, no. 7, p. 075014, Apr. 2024.

[95] A. Davlataliev, J. Rayimbaev, F. Abdulkhamidov, Z. Stuchlik, and A. Abdujabbarov, "Circular motion and collisions of charged spinning particles near Kerr Newman black holes," *Phys. Dark Univ.*, vol. 46, p. 101590, 2024.

[96] A. Davlataliev, B. Narzilloev, I. Hussain, A. Abdujabbarov, and B. Ahmedov, "Charged and magnetized particle motion around a static black hole in the Starobinsky–Bel–Robinson gravity," *Eur. Phys. J. C*, vol. 84, no. 7, p. 694, 2024.

[97] V. I. Danchev and D. D. Doneva, "Constraining the equation of state in modified gravity via universal relations," *Phys. Rev. D*, vol. 103, no. 2, p. 024049, Jan. 2021.

[98] T. Baker and I. Harrison, "Constraining scalar-tensor modified gravity with gravitational waves and large scale structure surveys," *JCAP*, vol. 2021, no. 1, p. 068, Jan. 2021.

[99] G. Carullo, "Enhancing modified gravity detection from gravitational-wave observations using the parametrized ringdown spin expansion coeffcients formalism," *Phys. Rev. D*, vol. 103, no. 12, p. 124043, Jun. 2021.

[100] A. Stepanian, S. Khlghatyan, and V. G. Gurzadyan, "Black hole shadow to probe modified gravity," *Eur. Phys. J. Plus*, vol. 136, no. 1, p. 127, Jan. 2021.

[101] G. Dvali and M. Zaldarriaga, "Changing α with Time: Implications for Fifth-Force-Type Experiments and Quintessence," *Phys. Rev. Lett*, vol. 88, no. 9, p. 091303, Mar. 2002.

[102] V. V. Kiselev, "Quintessence and black holes," *Classical and Quantum Gravity*, vol. 20, no. 6, pp. 1187–1197, Mar. 2003.

[103] J. M. Toledo and V. B. Bezerra, "The Reissner-Nordström black hole surrounded by quintessence and a cloud of strings: Thermodynamics and quasinormal modes," *Int. J. Mod. Phys. D*, vol. 28, no. 1, p. 1950023, Jan. 2019.

[104] M. B. Hindmarsh and T. W. B. Kibble, "Cosmic strings," *Rept. Prog. Phys.*, vol. 58, no. 5, pp. 477–562, May 1995.

[105] M. Sharif and M. Shahzadi, "Neutral Particle Motion around a Schwarzschild Black Hole in Modified Gravity," *J. Exp. Theor. Phys.*, vol. 127, no. 3, pp. 491–502, Sep. 2018.

[106] ——, "Particle dynamics near Kerr-MOG black hole," *Eur. Phys. J. C*, vol. 77, no. 6, p. 363, Jun. 2017.

[107] J. L. Synge, "The escape of photons from gravitationally intense stars," *Mon. Not. R. Astron. Soc.*, vol. 131, p. 463, Jan. 1966.

[108] J. P. Luminet, "Image of a spherical black hole with thin accretion disk." *Astron. Astrophys.*, vol. 75, pp. 228–235, May 1979.

[109] J. M. Bardeen, "Rapidly rotating stars, disks, and black holes." in *Black Holes (Les Astres Occlus)*, C. Dewitt and B. S. Dewitt, Eds., Jan. 1973, pp. 241–289.

[110] M. A. Markov and V. F. Mukhanov, "De Sitter-like initial state of the universe as a result of asymptotical disappearance of gravitational interactions of matter." *Nuovo Cimento B Serie*, vol. 86B, no. 1, pp. 97–102, Jan. 1985.

[111] M. Reuter, "Nonperturbative evolution equation for quantum gravity," *Phys. Rev. D*, vol. 57, no. 2, pp. 971–985, Jan. 1998.

[112] A. Bonanno, T. Denz, J. M. Pawlowski, and M. Reichert, "Reconstructing the graviton," *SciPost Phys.*, vol. 12, no. 1, p. 001, Jan. 2022.

[113] L. Stella and M. Vietri, "Lense-thirring precession and quasi-periodic oscillations in low-mass x-ray binaries," *The Astrophysical Journal Letters*, vol. 492, pp. L59–L62, 1998.

[114] ——, "khz quasi-periodic oscillations in low-mass x-ray binaries as probes of general relativity in the strong-field regime," *Physical Review Letters*, vol. 82, pp. 17–20, 1999.

[115] W. K. M. A. Abramowicz, "A precise determination of angular momentum in the thin disk around a black hole," *Astronomy & Astrophysics*, vol. 404, pp. L21–L24, 2003.

[116] G. Török, M. A. Abramowicz, W. Kluźniak, and Z. Stuchlík, "The orbital resonance model for twin peak khz quasi periodic oscillations in microquasars," *Astronomy & Astrophysics*, vol. 436, pp. 1–8, 2005.

[117] D. Foreman-Mackey, D. W. Hogg, D. Lang, and J. Goodman, "emcee: The MCMC Hammer," *Publications of the Astronomical Society of the Pacific*, vol. 125, no. 925, p. 306, Mar. 2013.

[118] C. Liu, H. Siew, T. Zhu, Q. Wu, Y. Sun, Y. Zhao, and H. Xu, "Constraints on the rotating self-dual black hole with quasi-periodic oscillations," *J. Cosmol. A. P.*, vol. 11, p. 096, 2023.

[119] F. Abdulkhamidov, P. Nedkova, J. Rayimbaev, J. Kunz, and B. Ahmedov, "Parameter constraints on traversable wormholes within beyond Horndeski theories through quasiperiodic oscillations," *Phys. Rev. D*, vol. 109, no. 10, p. 104074, 2024.

[120] A. Davlataliev, F. Atamurotov, A. Abdujabbarov, N. Juraeva, and V. Khamidov, "Constraints on Schwarzschild-like black hole from QPOs data," *Phys. Dark Univ.*, vol. 46, p. 101603, 2024.

[121] G. Mustafa, E. Demir, A. Davlataliev, H. Chaudhary, F. Atamurotov, and E. Güdekli, "Observational signature of QPOs with particle motion around non-commutative Schwarzschild black hole surrounded by perfect fluid dark matter," *Phys. Dark Univ.*, vol. 46, p. 101644, 2024.

[122] A. Davlataliev, B. Narzilloev, I. Hussain, A. Abdujabbarov, and B. Ahmedov, "Quasi periodic oscillations around Kerr-type black hole in the Starobinsky–Bel–Robinson theory of gravity," *Phys. Dark Univ.*, vol. 46, p. 101569, 2024.

[123] H. Hoshimov, A. Davlataliev, F. Atamurotov, A. Abdujabbarov, and A. Övgün, "Particle dynamics and quasi-periodic oscillations in the Dyonic ModMax: Constraint using quasars data," *JHEAp*, vol. 45, pp. 306–315, 2025.

[124] S. E. Motta, T. Belloni, L. Stella, G. Pappas, J. Casares, A. T. Muñoz-Darias, M. A. P. Torres, and I. V. Yanes-Rizo, "Black hole mass and spin measurements through the relativistic precession model: XTE J1859+226," *Mon. Not. R. Astron. Soc, Volume 517, Issue 1, pp.1469-1475*, vol. 517, no. 1, pp. 1469–1475, Nov. 2022.

[125] A. Urmanov, H. Chakrabarty, and D. Malafarina, "Observational properties of regular black holes in Asymptotic Safety," *arXiv e-prints*, p. arXiv:2504.12072, Apr. 2025.